Thesis

The Structure and Solidification Behaviour of a Mould Slag Used in Continuous Casting of Steels

Márton Áron Lengyel

Supervisors:

Dr. Ir. Begoña Santillana (Tata Steel)

Dr. Ir. S. Erik Offerman (TU Delft)

Dr. Ir. Georgy Filonenko (TU Delft)





Acknowledgement

First and foremost, I would like to express my deepest gratitude to Dr. Begoña Santillana and Dr. Alma I. Olivos-Suarez for their invaluable guidance and support during my work at Tata Steel. Their insights and encouragement have been instrumental in shaping this thesis. Tata Steel was an encouraging company to work at my thesis therefore I would like to thank the whole company for the opportunity. I am also sincerely grateful to Dr. Ir. S. Erik Offerman and Dr. Ir. Georgy Filonenko for their thoughtful feedback, which significantly enhanced the quality of my work. A special thank you goes to Deborah Ganzinga-Jurg for her invaluable assistance with the Raman spectroscopy measurements, and to Fons Vermeulen for his help with the FactSage calculations, which greatly contributed to this research. Lastly, I would like to thank my friends and family for their support throughout my university journey. Their encouragement has been a constant source of strength and motivation for me.

Contents

Acknowledgement ii
Abstract iii
List of Tables iv
List of Figures v
Nomenclature vii
1. Introduction 1
1.1. Continuous casting 1
1.1.1. Process 1
1.1.2. Quality and production problems 2
1.1.3. Heat transfer 3
1.2. Mould slags 4
1.2.1. Purpose 4
1.2.2. Manufacturing method 5
1.2.3. Structure 6
1.2.4. Heat transfer calculations 8
1.2.5. Future developments 8
1.3. Measurement methods 9
1.3.1. Physical state change measurements 9
1.3.2. Material structure measurements 10
1.4. Research Goals 13
2. Material 14
2.1. Mould powder 14
2.2. Sample holder 15
3. Experiments 16
3.1. Raman Spectroscopy 17
3.1.1. Sample preparation 17
3.1.2. Raman spectroscopy 17
3.1.3. Optical microscopy 19
3.1.4. Calculation methods 20
3.2. X-Ray Diffraction 20
3.3. Scanning Electron Microscopy 21
3.4. Thermodynamic calculations 21
4. Results 21

4.1. Raman Spectroscopy 21
4.1.1. Room temperature results 21
4.1.2. Results of high temperature measurements 25
4.2. X-Ray Diffraction 29
4.3. Scanning electron microscopy 30
4.4. Thermodynamic calculations 33
5. Discussion 34
5.1. Structure of the mould slags 34
5.1.1. Room temperature structure 34
5.1.2. High temperature structure 37
5.1.3. Phase formation 39
5.2. Characterisation methods 40
5.3. Influence on the casting process 41
6. Conclusion and recommendations 42
References 44
Appendix 1: Raman spectroscopy measurement details 48
Appendix 2: Sample holder material selection 50
Appendix 3: Raman spectrum band assignment proposals 51
Appendix 4: S2 Raman spectroscopy measurement results 54
Appendix 5: X-ray photoelectron spectroscopy results 56

Abstract

Continuous casting is the dominant manufacturing method of steels, accounting for over 90% of global steel production. Mould slags, which are calcium silicate glasses, play a crucial role in this process due to their multifunctional purpose, directly impacting the safety, quality, and efficiency of steel production. As the steel industry transitions toward greener practices, new challenges arise, including the need for fluorine-free mould slags to meet increasingly stringent safety and environmental regulations. Historically, mould powder development has relied heavily on trial-and-error approaches, limiting the development rate of these materials for new demands.

This thesis is part of a broader research effort aimed at understanding the structural transformations that drive the desired material properties of mould slags. In this study, various characterization techniques—such as X-ray diffraction (XRD), scanning electron microscopy (SEM), and high-temperature Raman spectroscopy (RS)—were employed to investigate the structure of an industrial mould slag, with a focus on its heat transfer properties. Samples were melted and then solidified followed by three different isothermal holding temperatures to replicate the thermal cycling experienced during casting.

The multi-method characterization revealed that the industrial mould slag (S1) consists of three distinct phases: cuspidine, combeite, and a glassy matrix. These phases were present regardless of the isothermal holding temperature. The microstructure after solidification featured large faceted cuspidine crystals embedded within a mixture of smaller dendritic combeite crystals and the glassy phase. High-temperature RS measurements showed that the formation kinetics of the S1 mould slag were faster than anticipated based on previous research.

This highlights the necessity of multi-method characterization, and not to rely only on the chemical composition to fully understand mould slags and adapt them to future industry requirements. While there is room for improving the accuracy of the utilized technique, high-temperature RS measurements have demonstrated their value in mould slag research and, with further refinement, hold the potential to unlock new research opportunities.

List of Tables

Table 1 Most common mould powder raw materials [7].....6
Table 2 Chemical composition of mould powders as given by the manufacturer.....14
Table 3 Mineralogical composition of mould powder S1 in wt% measured by Tata Steel.....15
Table 4 Melting trajectory of S1 mould powder according to DIN 51730 measurement measured by the manufacturer.....15
Table 5 Heat treatment and Raman measurement specifications 16
Table 6 Raman spectroscopy measurement setup 19
Table 7 Rietveld full profile refinement analysis results of the S1 mould slag samples after the 400℃, 650℃, and 900℃ heat treatments 30
Table 8 Overall crystalline ratio results by the different characterisation methods 32
Table 9 Calculated cuspidine and combeite phase fractions of S1 mould slag at high temperatures.....33
Table 10 Phase fractions, at the three experimentally examined temperatures, according to the thermodynamical calculations 36
Table 11 Detailed Raman spectroscopy measurement environmental details.....48
Table 12 Temperature programs and follow-up experiments of each heat-treated sample.....49
Table 13 Proposed sample holder material options and their relevant material properties.....50
Table 14 S2 mould powder composition 54

List of Figures

Figure 1 The continuous casting process [3] 2
Figure 2 Schematic diagram of the continuous casting mould [7] 3
Figure 3 The transformation steps from minerals to mould slag 5
Figure 4 Granulated mould powder particles under an optical microscope [7] 5
Figure 5 Schematic drawing of silica structures with different number of bridging oxygen atoms and the structure's Q number [11] 7
Figure 6 TTT diagram indicating phases that form at distinct times and temperatures [14] 8
Figure 7 Viscosity of mould slags as a function of reciprocal temperature [20] 9
Figure 8 Images taken during a melting point determination measurement according to DIN 51730 [21] 10
Figure 9 Rayleigh and Raman scattering [22] 11
Figure 10 Raman spectrum of deionized water at different temperatures [25] 12
Figure 11 Raman spectra recorded from an industrial mould slag sample at different temperatures [10] 13
Figure 12 The experimental heat cycle plan with measurement points and characterisation techniques 16
Figure 13 InSpect confocal Raman microscope [33] 17
Figure 14 Raman spectrum measured with the 785 nm laser compared with the RRUFF database Raman spectrum of cuspidine measured with a 780nm laser [37] 22
Figure 15 Measured Raman spectra type 1 examples: raw and baseline corrected spectra of E4 m25/21 23
Figure 16 Measured Raman spectra type 2 examples: raw and baseline corrected spectra of E4 m25/25 23
Figure 17 High temperature Raman spectra examples of S1 a: 400℃ b:650℃ c:900℃ 26
Figure 18 The average peak intensity changes through the heat treatment of the different Si-O Raman bands (Q1, Q2) 27
Figure 19 Raman spectrum of the S1 mould slag at 25˚C and 650˚C measured with a closed measurement cell 28
Figure 20 XRD results of the S1 mould slag at room temperature after: A: 400℃, B: 900℃, C: 650℃ heat treatment 29
Figure 21 Left: atomic contrast SEM image E2 (650℃), Right: chemical composition of E2 (650℃) measured by SEM 30
Figure 22 Elemental distribution for selected elements of E2 (650℃) measured with SEM-EDS 31
Figure 23 Detailed atomic contrast SEM image of E2 (650℃) 31
Figure 24 SEM atomic contrast images of the microstructure of the S1 mould slag after heat treatments at A: 400℃, B: 650℃, C: 900℃ temperatures 32
Figure 25 The phases and phase fractions predicted by thermodynamic calculations of the S1 mould slag at different temperatures 33
Figure 26 Left: optical image Right: Raman intensity at 911 [cm-1] (Q1 peak of Si-O) of E5 at room temperature 35
Figure 27 Internuclear spacing described by the Morse potential [45] 38
Figure 28 Temperature dependence of the Si-O (Q1) bond shown by the peak position change in the Raman spectrum 38

Figure 29 Relative Raman peak intensity changes of two different types of Si-O bonds (Q1, Q2) during isothermal holding.....40
Figure 30 S2 Type 4 Raman spectra of S2 mould slag measured with 488nm laser.....52
Figure 31 Type 2 Raman spectra of S2 mould slag measured with 488nm laser.....52
Figure 32 Type 2 and type 4 Raman spectra of the S" mould slag, measured with 633nm laser 53
Figure 33 Type 1 Raman spectra of S2 mould slag.....55
Figure 34 Type 2 Raman spectra of S2 mould slag.....55
Figure 35 XPS measurement results of E2 sample of the S1 mould slag after a 650˚C heat cycle 56

Nomenclature

SEN – submerged entry nozzle

TTT – time-temperature transformation diagram

DIN – Deutsches Institut für Normung (German Institute for Standardization)

XRD – X-ray diffraction

SEM – scanning electron microscopy

BSE – backscattered electrons

SE – secondary electron

EDS – energy-dispersive X-ray spectroscopy

RS – Raman spectroscopy

XPS – X-ray photoelectron spectroscopy

OM – optical microscopy

DFT – density functional theory

RT – room temperature

MLR – multi-linear regression

Si – Silicon

O – Oxygen

Ca – Calcium

Al – Aluminium

Na – Sodium

K – Potassium

Ni – Nickel

F – Fluorine

Li – Lithium

B – Boron

C – Carbon

Co – Cobalt

1. Introduction

Steel is a versatile and widely used material in both construction and engineering applications. Its extensive utilisation is possible due to its relatively low price and wide range of properties. The steel industry as a whole is going through extensive changes worldwide. In Asia and the developing countries this change is fuelled by the growth in demand [1], while in developed countries like Japan, United States and in Europe, by the ever-tightening environmental regulations which require a so-called green transition [2]. During the green transition, the whole iron- and steelmaking process will be changed from a fossil fuel (coal) based process to an environmentally friendly hydrogen-based process.

Flat steel product manufacturing usually consists of five steps. These are: primary steelmaking, secondary steelmaking, casting, rolling, and finally forming. Heat treatment steps are also commonly added in between these steps to achieve the required properties. Changing the primary steelmaking process due to the green transition will inevitably change the following steps, too. The new green steel grades will presumably have a new chemical composition which will lead to different cooling requirements in the casting step. More than 90% of all steels is produced through the continuous casting process [3]. In continuous casting mould slags influence the heat transfer in the mould thus the cooling speed of the steel. Therefore, mould slag developments are in the focus not only because of the changes in the heat transfer requirements, but also because they fulfil many other roles during casting. Mould slags influence both the safety and the quality of continuous casting therefore their improvement yields significant gains in steel production.

1.1. Continuous casting

1.1.1. Process

The goal of the continuous casting process is to fully solidify the liquid steel into a continuous two-dimensional shape which can be either a slab, bloom, billet or even a near-net shape one like a beam blank or a thin slab. Apart from a few specialized parts like the submerged entry nozzle (SEN) and the casting mould, the general build-up of the continuous casting machine is uniform. The liquid steel arrives to the continuous casting machine in a refractory lined ladle from the secondary steelmaking step. This ladle is then placed upon the rotating turret which moves it on top of the tundish. The liquid steel flows first from the ladle to the tundish and then to the mould. The tundish acts as a liquid reservoir during ladle changes and thus ensures a continuous flow of steel to the mould (Figure 1) [4].

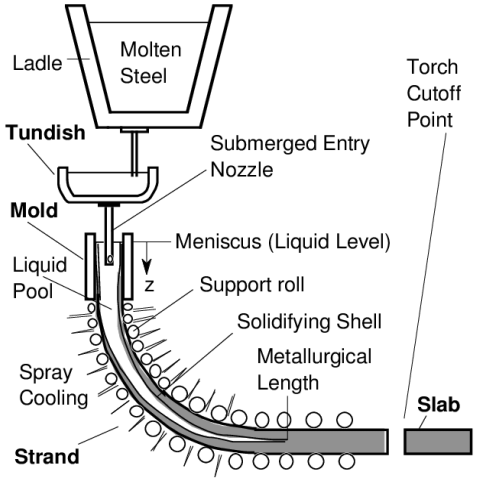

Figure 1 The continuous casting process [3]

Liquid steel flows into the water-cooled copper mould through the submerged entry nozzle. The steel is not in direct contact with the mould because it is separated by a mould slag layer. Mould powder is added to the top of the liquid steel in the mould. As this powder melts, it forms a liquid which is called mould slag. Mould slags have a multipurpose role, because they lubricate the mould – steel strand gap, control the heat transfer across the gap, and perform other tasks too which will be discussed later. The liquid steel starts to solidify inside the mould, forming a continuously growing steel shell. After the mould exit, the steel shell must be thick enough to bear the ferrostatic pressure of the liquid steel [3, 4].

After the mould exit the steel shell is first bent and then unbent by the support rollers, to get to a horizontal position to decrease the machine height. During the bending and unbending the steel shell is further cooled by the rollers, water sprays, and by the surrounding air. The distance to the point where the steel shape is fully solid is called the metallurgical length. After the metallurgical length the continuous steel shape is cut into pieces by an oxy-acetylene torch. The continuous casting process ends here after the cutoff, and the steel is transported to the site of the next steps [3, 4].

1.1.2. Quality and production problems

Production challenges can vary widely, from quality issues to safety risks. The most critical issue is a breakout, because a single breakout can cost the manufacturer up to one million Euros and, more importantly, it can endanger the safety of workers near the continuous casting machine. A breakout occurs when the solidified steel shell lacks sufficient strength after the mould exit where it is no longer supported from all sides, allowing the ferrostatic pressure of the still-liquid steel to rupture the shell, causing the steel to spill out. This can result in fatal injuries to the personnel, severe damage to the machine, and prolonged production downtime. The local weakening of the steel shell is caused by uneven heat extraction in the mould. Mould slags are responsible for controlling the in – mould heat transfer, therefore a wrong mould slag can cause a breakout by not cooling the steel shell evenly [5, 6].

Another issue is a sticker, which develops within the copper mould and can eventually lead to a breakout too. Stickers occur when the mould slag layer becomes too thin or even disappears entirely, causing the steel to adhere to the mould surface. The relative movement

between the strand and the mould then damages the solidified shell, leading to an uneven and weakened shell that may bulge and rupture after exiting the mould. Stickers happen where the mould slags thin out or completely disappear from the mould – shell gap, therefore wrong mould slags can cause this type of error too [5, 6].

Inclusions and slag entrapments belong to another category of quality issues. These defects arise when the mould slag's viscosity and chemistry are not properly aligned with the specific steel grade being processed. If the surface tension is too low, slag particles can enter the liquid steel, and as the steel solidifies, these particles become inclusions [5, 6].

Other quality concerns include transverse and longitudinal cracks, as well as surface defects. Although these issues vary in nature, they are all connected with the solidification process and the heat extraction within the mould. Each steel grade has its maximum cooling rate that it can tolerate without cracking. Cracking is caused by the thermal stresses that occur during cooling. To avoid cracking, each steel type must be cast with the appropriate cooling speed, therefore the right mould slag which provides the required cooling speed. [5, 6].

1.1.3. Heat transfer

Heat transfer is the single most important phenomenon during the continuous casting process because it controls the cooling of the steel, which determines the quality, safety and speed of the process. Heat transfer or cooling-wise the continuous casting process is taking place in two regions: the primary and secondary cooling zone. The primary cooling zone consists of the mould, the secondary cooling zone includes everything after the mould exit like the water sprays rollers etc. Although part of the inner part of the steel slabs solidifies in the secondary cooling region, most of the problems originate from the primary cooling zone, thus the focus is on the primary cooling zone in this thesis. The most common continuous casting machine is the slab caster which has a cuboid mould shape. This, and other shapes, are usually divided into a vertical and horizontal component. [3, 4].

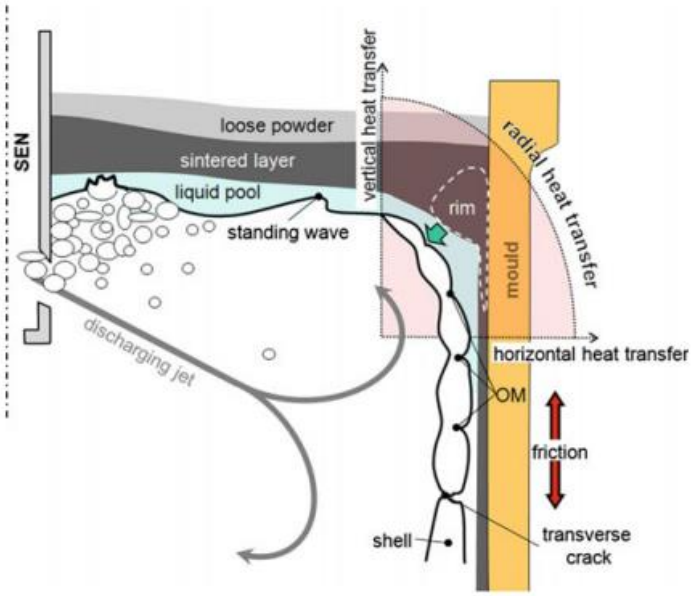

Figure 2 Schematic diagram of the continuous casting mould [7]

Heat transfer is a type of energy transfer phenomenon where the local temperature is determined by the amount of energy that can be transferred and the transfer rate. The transfer rate is largely influenced by the materials and their volume that lie between the heat source (liquid steel) and the cooling medium (water/air). In the vertical direction this volume is usually divided into the layers of the liquid mould slag, sintered mould powder or transition layer, and the mould powder layer. In the horizontal direction, these layers include the solidified steel shell, the mould slag layer and the airgap layer going from the liquid steel to the outside direction. In both directions, the mould slag plays an influential role. In the horizontal direction the slag layer is responsible for the largest thermal barrier. Despite its low thickness (a typical slag layer in continuous casting is less than 4 mm thick), a mould slag layer can show several hundreds of degrees temperature difference between its two sides. This means that by improving the control of the material parameters, that determine the overall heat transfer coefficient of the mould slag, the control over the heat transfer phenomena can also be improved. This improved control can be translated to better safety, quality and production rate thus gaining a better understanding of the mould slag's heat transfer behaviour can improve the whole continuous casting process [7].

1.2. Mould slags

In the early days of continuous casting, casting oils, like rapeseed oil, were used instead of mould slags to separate the liquid steel from the copper mould during casting. These casting oils provided sufficient lubrication in the steel strand – copper mould gap but a low casting speed and a high liquid steel pouring temperature had to be used due to their heat transfer behaviour which was not satisfactory for continuous casting. On the top of the mould (vertical mould level heat transfer) a good thermal insulation is needed, so the pouring temperature can be reduced. On the sides of the mould (horizontal mould level heat transfer) an even but changeable heat transfer behaviour is required from the lubricating agent. The ability to change the heat transfer rate is needed because different steel grades have different cooling requirements due to their thermal expansion coefficients. For example, plain carbon steels, which have a low thermal expansion coefficient, can be casted with a fast-cooling rate because they won't crack, but peritectic steels must be cast with a slow cooling speed to avoid cracking. Because of their superior heat transfer behaviour, mould powders slowly substituted the casting oils [7].

1.2.1. Purpose

Mould powders and slags have different, sometimes contradictory roles in the continuous casting process. These roles, without specific order are:

- Insulating the top of the liquid steel in the powder form
- Forming a continuous airtight liquid layer on top of the liquid steel to prevent steel oxidation
- Absorbing any remaining inclusions from the liquid steel
- Penetrating and lubricating the steel strand – copper mould gap
- Controlling the heat transfer rate in the strand – mould gap

These roles together determine the success and suitability of a given mould powder. The first requirement is fulfilled in the granulated powder form, the second third and fourth are fulfilled in the liquid slag form, while the last one is fulfilled during re-solidification of the mould slag.

The mould slag properties are important in all three states (powder, liquid slag, solid slag) but from the in-mould heat transfer point of view the re-solidified structure is the most important, therefore it will be further studied in this thesis [7].

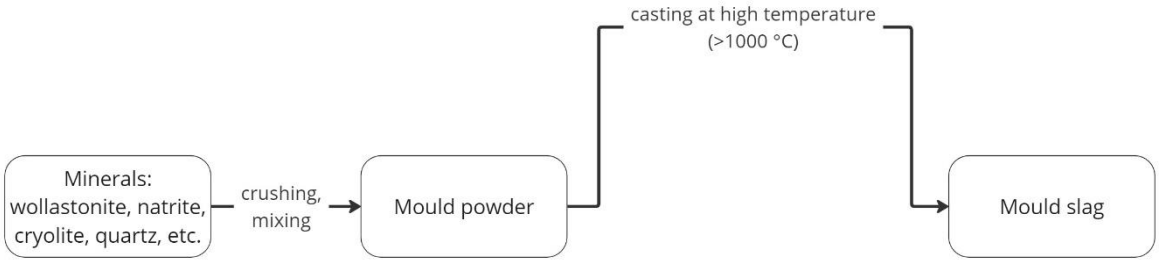

Figure 3 The transformation steps from minerals to mould slag

1.2.2. Manufacturing method

Mould powders are used in large quantities. Therefore, their production is a relatively simple and cheap process. The raw materials of the mould powders are minerals which are mined from open-pit mines in great quantities. These minerals are crushed and mixed according to a recipe. Although the chemical composition is kept between the boundaries set by the manufacturer, the original mineral type, the purity, and the presence of elements which are not part of the goal chemistry can vary from batch to batch. The variability is mainly due to the low price of these materials. After the mixing, a water based bonding agent is added to the mix, which is then sprayed into a heated chamber. The hot air in the chamber evaporates the water inside the mould powder droplets. This evaporation leads to the formation of a bubble which partly bursts due to the pressure of the steam, which leads to the hollow ball shapes of the mould powder granulates (Figure 4) [7].

Mould powders are also used in the non-granulated powder form, but more and more manufacturers are changing to the granulated form because the reduced dust levels in the plant and the better casting performance outweighs the higher costs.

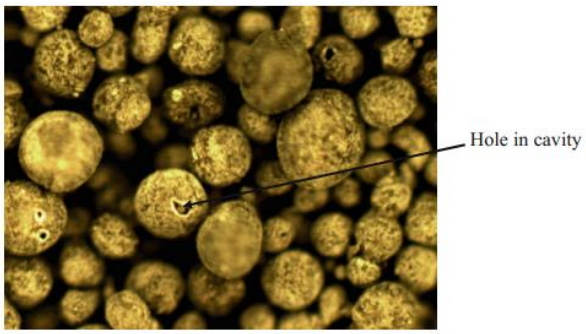

Figure 4 Granulated mould powder particles under an optical microscope [7]

Some of the most common mould powder raw materials are summarised in Table 1.

Table 1 Most common mould powder raw materials [7]

Chemical formula	Mineralogical origins
SiO_2	Feldspar, wollastonite, perlite, spodumene, cullet (crushed glass), fly ash, quartz dust
CaO	Lime, limestone, calcite, wollastonite, cement, slags, gypsum, calcium silicate.
Al_2O_3	Mullite, corundum
Na_2O/K_2O	Natrite, potash, feldspar, sodium silicate, cullet (crushed glass)
F	Fluorinespar, sodium fluorineide, cryolite, sodium hexafluorineosilicate
Li_2O	Spodumene, lithium carbonate
C	Carbon black, coke dust, fine graphite, fly ash

1.2.3. Structure

Mould slags usually are calcium silicate glasses, but special or experimental slags can be any other type of glass, too. In the generic fluorine (F) containing mould slags the main building block is the silicon (Si) tetrahedron where the Si cation is surrounded by four oxygen (O) anions. These O atoms can be either bridging or non-bridging O atoms in the tetrahedron (Figure 5). A bridging O atom is bonded to two Si atoms and tetrahedrons thus forming a network of tetrahedrons. The number of bridging O atoms will determine the complexity and thus the properties of the mould slags therefore a Q number is commonly assigned to the silicon tetrahedrons. The Q number states how many bridging oxygen atoms are connected to the Si atom in each tetrahedron [9]:

- Q^4: 4 bridging oxygen atoms per silicon
- Q^3: 3 bridging and 1 non-bridging oxygen atom per silicon
- Q^1: 2 bridging and 2 non-bridging oxygen atoms per silicon
- Q^1: 1 bridging and 3 non-bridging oxygen atoms per silicon
- Q^0: 4 non-bridging oxygen atoms per silicon

The Q^0, Q^1, Q^2, Q^3, Q^4, numbers represent the presence of silica monomers, dimers, chains, sheets, and 3 D structures, respectively. The ratio of the Q numbers is in direct relation with the properties. For example, a decrease in the Q^3/Q^2, or the Q^3/Q^0 ratio will result in a decreased viscosity of the melt, because chains and monomers can flow more easily than sheets in the melt [10].

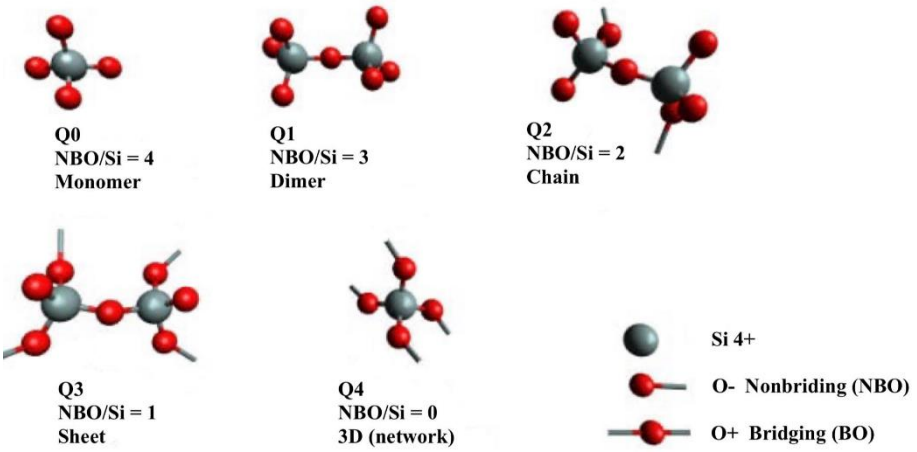

Figure 5 Schematic drawing of silica structures with different number of bridging oxygen atoms and the structure's Q number [11]

Network breakers, formers and fluxes are also added to the mould powders to modify the mould slags behaviour. Network breakers bond to the O^- atoms, changing them to non-bridging oxygens, thus simplifying the network structure. Network formers can form their own tetrahedron enhancing the number of bridging oxygen atoms, and the complexity of the structure. Fluxes do not bond directly with the O atoms thus they do not modify the network structure directly. Due to the complex interactions of the different cations and anions, specific elements, like aluminium, can act both as a network breaker and a network former depending on the overall chemistry of the mould slag [7, 8].

During the continuous casting process the mould slags resolidify in the strand – mould gap. During this solidification the mould slags can form an amorphous glass, an ionic crystalline solid structure, or a mixture of the two. The two most widely accepted rule sets for amorphous glass and crystalline solid formation of ionic melts are Zachariasen's [12] and Pauling's [13] rules respectively. In general, the chemical composition determines if, and what type of crystalline structures can be formed from the given mould slag melt (thermodynamics), and the cooling speed determines if and how fast these will form (kinetics). This is because any material can form an amorphous glass if it is cooled fast enough [9], therefore the chemistry alone is not enough to determine the resolidified structure of mould slags. The combined effect of the kinetics and thermodynamics of a mould slag crystallisation can be depicted in time temperature transformation (TTT) diagrams (Figure 6) [14]. These diagrams show the formed phases and sometimes their ratio. Only a few TTT diagrams have been published in the literature about industrial mould slags. This is because they cannot be obtained accurately through theoretical calculations due to their complex nature, plus obtaining them experimentally is expensive and time consuming. The mould powder's chemistry can change even if it is namely the same powder, plus a single steel plant can use several different mould powders for a single steel type, therefore material characterisation can also improve the quality control of such materials.

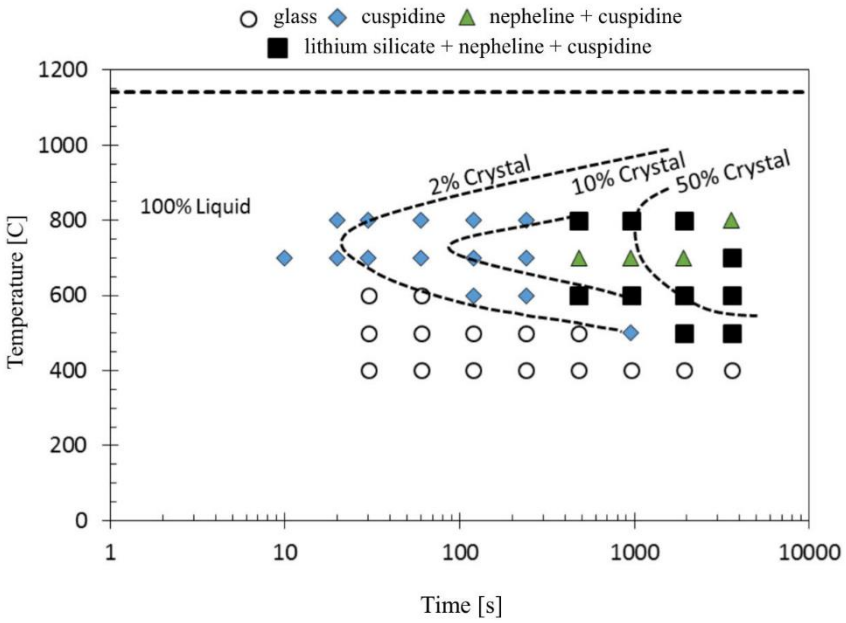

Figure 6 TTT diagram indicating phases that form at distinct times and temperatures [14]

1.2.4. Heat transfer calculations

In heat transfer calculations the mould slag layer is usually divided into three sublayers. These are the liquid, crystalline, and amorphous slag layers. This is done because these three phases have vastly different heat transfer coefficients and their thickness (relative ratio) changes along the mould height. Depending on the temperature, composition and structure of the mould slags the thermal conductivity can hugely vary in the range of 0,01-2,5 $Wm^{-1}K^{-1}$ [7].

Much research has been focused on determining the effect of mould slag properties on the heat transfer coefficients [15-18]. In conclusion these are the four most influential parameters on the heat transfer behaviour of mould slags:

- Phases (lattice or phonon conduction)
- Phase ratios (radiative and lattice or phonon conduction)
- Crystal size and distribution (radiative and lattice or phonon conduction)
- Presence and distribution of transition metal oxides (radiative heat conduction)

1.2.5. Future developments

There are two challenges why mould slag research and development must be intensified in the following years. One of the challenges is the green transition of the steel industry which will produce new steel grades with new cooling requirements. The other challenge is constituted by the strict safety regulations which push the steel industry towards using low fluorine and soon F-free mould powders [19]

Both developments require extensive change to the mould slag chemistries while keeping or improving the performance of currently used mould slags. This huge change requires the industry to switch from the previously used method of try and error-based mould slag development to a material science based scientific path. In the next subchapter, the

measurement methods that are used in the field of mould slag research are summarised to explore how this step can be taken.

1.3. Measurement methods

Several dozens of methods are used in mould slag research but only those will be discussed in more detail which are used to determine one of the heat transfer behaviours determining structural parameters (phases, phase ratio, morphology, transition metal oxide distribution).

1.3.1. Physical state change measurements

The structure of any material can be measured directly or indirectly. Indirect measurements are those, when a physical property, which is directly linked to a structure change, is measured and the structure change is observed or calculated through this. Viscosity is one of these indirect measurements. The solidification temperature of mould slags is commonly measured through a viscosity measurement. The viscosity is logged at different temperatures and plotted. The solidification temperature is determined by finding the temperature where viscosity suddenly increases (Figure 7) [20].

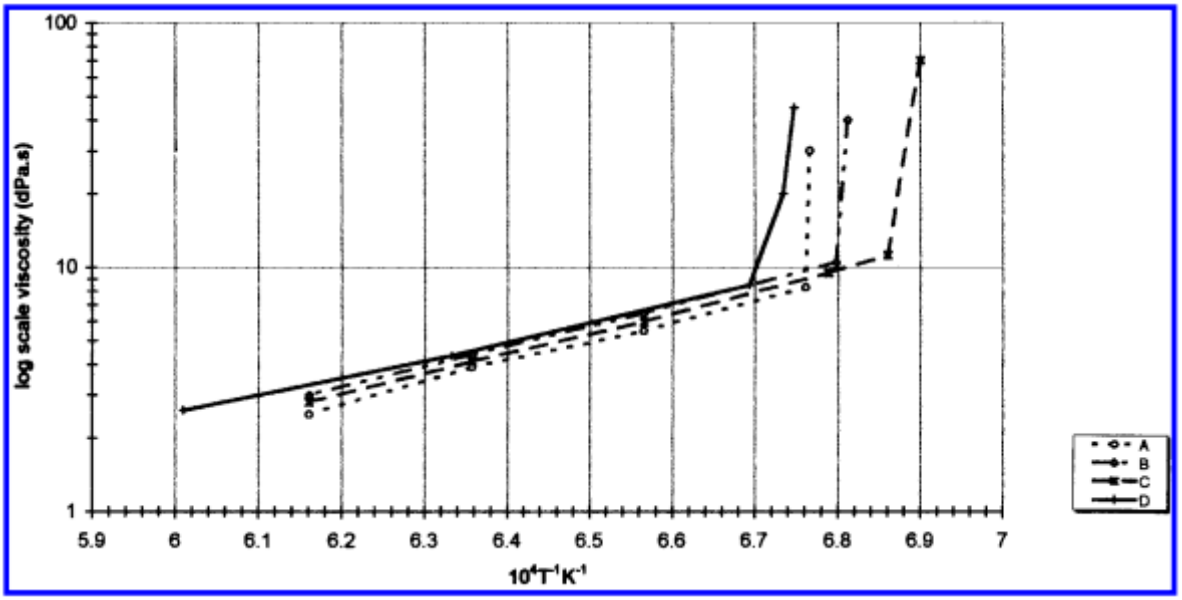

Figure 7 Viscosity of mould slags as a function of reciprocal temperature [20]

Although this temperature is a good approximation for most cases, but it doesn't represent the exact temperature where the actual physical change (change in atomic bonding) takes place, only its result. For the most used mould powders Shridar's equation [20] can predict this point but it is an empirical equation thus not applicable for newly developed, structurally different (F-free) mould slags.

Another commonly used indirect structure measurement method is the standardised ash melting behaviour test, DIN 51730. This method has been developed to test ashes but is also used for mould powders. In fact, this is the method how most of the mould powder manufacturers determine the softening, melting, and fluidity points which are presented on the mould powder data sheets. This method is a visual inspection method where a standard sized cube is formed from the powder and this cube is melted. As the temperature increases

the shape of the cube changes (Figure 8) [21]. The melting and other relevant points are determined from the images taken through the heating process.

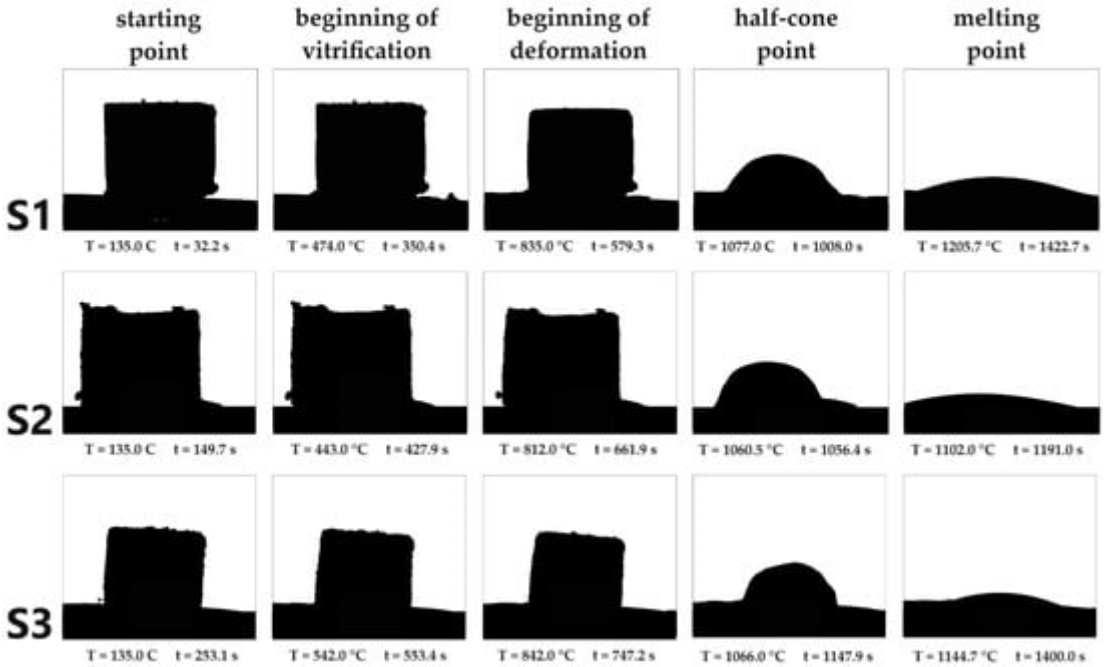

Figure 8 Images taken during a melting point determination measurement according to DIN 51730 [21]

This method, similarly, to the viscosity measurement is a relatively easy and simple way of determining the overall melting point but it gives no information about the individual constituent's melting points, how the exact state change happens, etc. To understand the structure and the structure changes of mould slag's direct characterisation methods which observe the structure of the materials should be used.

1.3.2. Material structure measurements

X-Ray diffraction

Direct structure measurements characterise bonds or atomic spacings through a physical effect like diffraction or light scattering. X-ray diffraction (XRD) is an extensively used characterisation method in mould slag research. It can accurately identify the phases present (including the presence of transition metal oxides), and with a well set up Rietveld analysis it can also calculate the phase fractions. As this is a bulk measurement method, it cannot determine the morphology. XRD has been in use since the early 1900s by both metallurgists and geologists. As a result, a vast body of literature exists, containing detailed reports on nearly all known minerals and crystalline structures, making phase identification highly reliable. Most XRD devices can be equipped with a temperature cell which makes high temperature measurements possible, too. The data collection speed of most devices is relatively slow (it takes approximately 1 hour to get a detailed spectrum). This makes it difficult to follow phase transitions in situ. This problem can be overcome by preparing several samples with different thermal histories (heat treatments) and examining them after the phase changes have taken place. This was the method was utilized by Pearson et al. [14] to determine an industrial mould slag's solidification behaviour. Although this method is

effective, in practice it is too slow and expensive to be used industrially to examine several dozens of different mould powders effectively. Its other shortcoming (the inability to characterise morphology) can be overcome by using some other characterisation method like optical or scanning electron microscopy (SEM) in parallel [3, 7, 9].

Raman spectroscopy

Raman spectroscopy (RS) is a vibrational spectroscopy technique that measures the interaction of the sample materials with a laser in the visible spectrum. It measures the scattering of the excitation laser. The light scattered by the sample material can have a lower, identical or a higher energy level (wavenumber) than the excitation laser. The identical energy scattering is called Rayleigh scattering, the lower and higher energy scattering are called Stokes and anti-Stokes Raman scattering, respectively. The excitation laser can change the energy level of symmetric bonds to a higher or lower level, and this is the energy level change that is the cause of the Raman scattering (Figure 9) [22]. Rayleigh scattering is more dominant than Raman scattering, therefore properly filtering the Rayleigh scattering is important to achieve an accurate measurement. Each unique bond has its own energy level change, thus Raman scattering peak position, therefore it is possible to identify individual bonds and complex material structures from the Raman spectra if they are Raman active. Raman activity is proportional to the polarizability, therefore symmetric bonds with high polarizability are more easily detectable than lower polarizability ones [22]. The main building block of the mould slag's structure is the silicon tetrahedron, in which the Si-O bond is Raman active, which makes RS a suitable technique to study mould slags.

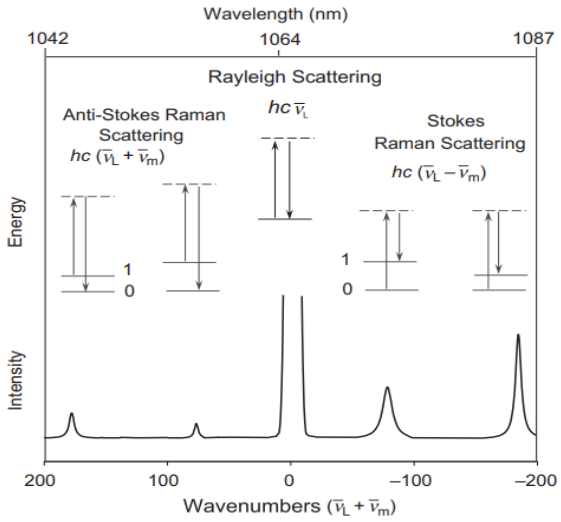

Figure 9 Rayleigh and Raman scattering [22]

During material identification, the collected Raman spectra's peaks are screened through databases to find the same spectra, therefore the measured material. The Raman spectra can be also theoretically calculated by classical or quantum mechanical theory for individual bonds [22], or by density-functional theory (DFT) for more complex systems [23]. Although these calculations are possible, due to their computationally demanding nature not all materials' Raman spectra have been calculated this way, and the computational Raman databases contain only a limited number of materials. Experimental Raman databases also exist, and due to the keen interest of the pharmaceutical industries and geologists in this technique the experimental databases contain vastly more materials. Therefore, detailed

mineral Raman databases like the RRUFF [24] create the basis for mould slag phase identification through RS.

All effects that modify the electron clouds that form the Raman active bonds will modify the Raman spectra, too, therefore this effect must be accounted for during spectra interpretation. For example, temperature changes both the position and the relative intensity of the Raman peaks (Figure 10) [25]. This and other effect creates the basis how changes could be examined with RS through a heat cycle.

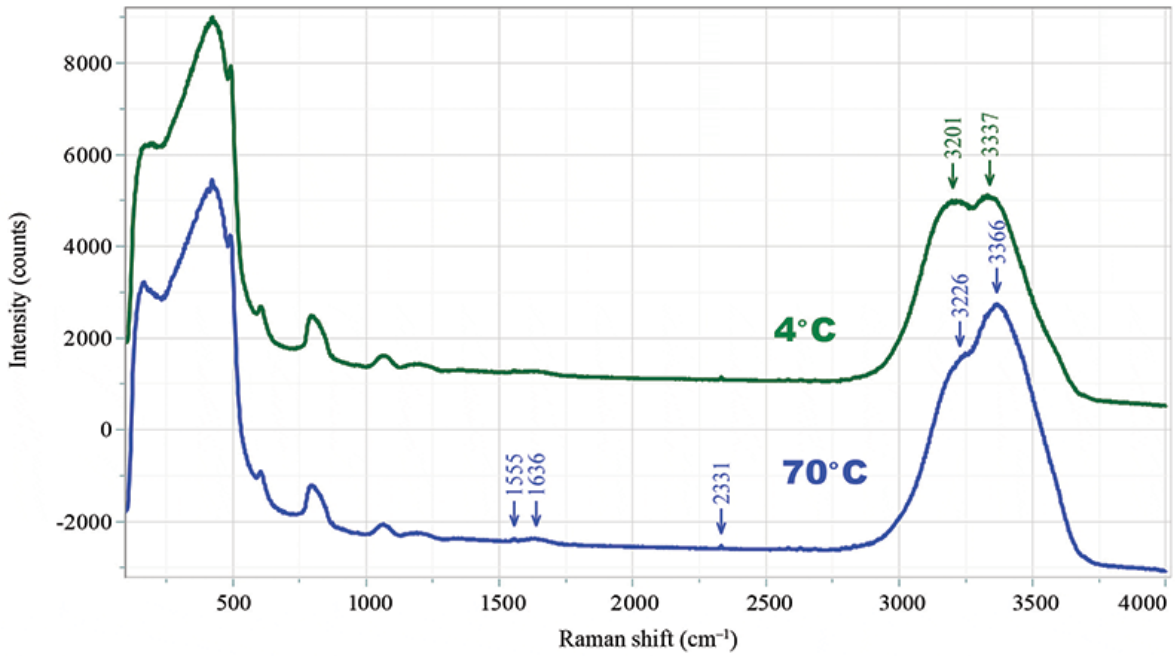

Figure 10 Raman spectrum of deionized water at different temperatures [25]

Although not extensively, Raman spectroscopy has been used in mould slag research in recent years [26-31]. It has been done both on industrial and synthetic samples and Zhang et al. [10] also performed high temperature in situ measurements with the technique (Figure 11). All this research has shown that the main building block of mould slags, the Si-O tetrahedron is visible in the Raman spectrum and depending on the local atomic configuration (number of bridging O atoms) the tetrahedrons are detected in four different peaks: Q^3, Q^2, Q^1 and Q^0.

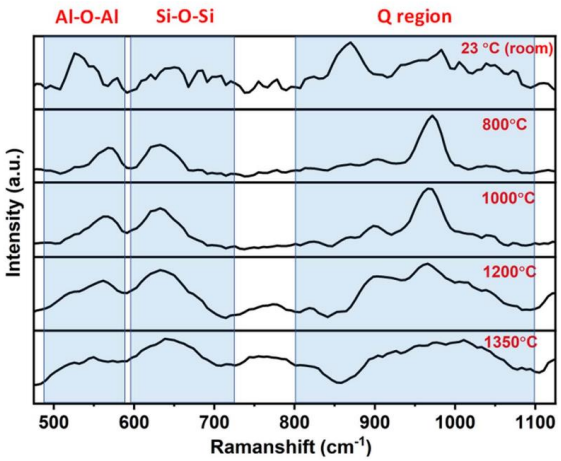

Figure 11 Raman spectra recorded from an industrial mould slag sample at different temperatures [10]

Park J. H. P. et al. [29] showed that there is a direct correlation between the Q_3/Q_2 ratio and slag viscosity, which paves a way to examine not only the heat transfer behaviour of mould slags, through phase identification etc., but also the lubrication behaviour through viscosity. Kim et al. [26], Matsushita et al. [27], and also Fan et al. [28], have proven that small amounts of additions can change the base network structure. This underlies the importance of examining industrial mould slag samples instead of synthetic samples for application feasibility research of new mould powders because <1wt% of boron (B) or another element can change the slag behaviour in such a way that will lead to production issues.

1.4. Research Goals

Mould slags play a multipurpose role in continuous casting of steels. These roles are to control the heat transfer in the mould, lubricate the steel shell, prevent steel oxidation, absorb inclusions and insulate the mould top. Heat transfer greatly influence the safety, quality and production rate of the casting process; therefore, this thesis focuses on this aspect. To better control the heat transfer, the structure and structure changes of the mould slags needs to be understood. To achieve a better heat transfer control, this thesis has set two research goals in the field of mould slag research.

The first goal is to characterise and study the four structural features of the S1 mould slag, that determine the mould slag's heat transfer behaviour. These four features are: 1. present phases, 2. phase ratios, 3. morphology, and 4. presence and distribution of transition metal oxides in the structure. These four features are examined by XRD (1,2,4) and SEM (3) after different heat treatments in the mould slag's working environment. This working environment has two stages, first in an air atmosphere on top of the mould, and second when it is in the mould – strand gap in vacuum in between 1000-400°C.

The second goal is to subsequently characterise the S1 mould slag by Raman microscopy to find out if the same heat transfer determining features can be determined in one experiment without splitting the experiment into different steps (heat treatment, XRD, SEM).

2. Material

2.1. Mould powder

In this research industrially used mould powders and mould slags are studied. The samples were taken from the same batch that was later used for steel manufacturing. The batch was delivered in a granulate form to the steel plant. The mould powders chemical composition, provided by the manufacturer, is given in weight % and calculated to mol % in Table 2.

Table 2 Chemical composition of mould powders as given by the manufacturer

	S1			
	Lower limit [wt%]	Upper limit [wt%]	Lower limit [mol%]	Upper limit [mol%]
CaO/SiO_2	*0.92*	1.04	1.05	1.06
SiO_2	32.5	34.5	25.5	23.8
CaO	32.0 (=CaO + MgO)	34.0	26.9 (=CaO + MgO)	25.1
MgO	0	0	0	0
Al_2O_3	2.5	3.5	1.2	1.4
Na_2O	11.5	13.0	8.7	8.7
K_2O	0	0	0	0
MnO	0	0.1	0	0.1
Fe_2O_3	0	1.0	0	0.3
F	7.0	8.5	17.4	18.5
C_{free}	*3.0*	*4.0*	11.8	13.8
CO_2	8.0	9.0	8.6	8.4
C_{total}	5.5	6.5	-	-

Mould powders are manufactured from open pit mined, crushed minerals. Although the chemical composition is kept relatively stable for a given mould powder, the mineralogical composition can vary, therefore it is also measured. The internal Tata Steel standard is a room temperature XRD measurement with subsequent Rietveld-analysis. The result of the analysis is summarised in Table 3.

Table 3 Mineralogical composition of mould powder S1 in wt% measured by Tata Steel

Name	**S1**
Silicates	
Quartz (SiO_2)	2
Wollastonite ($CaSiO_3$)	50
Diopside ($CaMgSi_2O_6$)	2
Anorthite $(Ca,Na)(Al,Si)_4O_8$	
Albite ($NaAlSi_3O_8$)	14
Fluorineites	
Fluorineite (CaF_2)	17
Carbonates	
Natrite (Na_2CO_3)	13
Calcite ($CaCO_3$)	2
Amorphous	0

Mould powders are multi-mineral composition materials therefore their melting takes place in a temperature range rather than at a single point. Therefore, their melting range is measured and presented according to the DIN 51730 standard. The melting trajectory of the specific powder is summarised in Table 4.

Table 4 Melting trajectory of S1 mould powder according to DIN 51730 measurement measured by the manufacturer

Name	**S1**
Softening temperature	1066
Melting temperature	1088
Fluidity temperature	1112

The life cycle of mould slags is shown in Figure 3. Mould slag form from the mould powder during the continuous casting process at high temperatures inside the casting mould. Any composition deviation of the minerals or mould powder therefore will directly affect the mould slag's behaviour during casting.

2.2. Sample holder

The sample holders available at Tata Steel for room and high temperature measurements are made of aluminium and tantalum, respectively. For general research purposes these materials are suitable as sample holders, but they cannot be used for mould slag research. Aluminium has a lower melting point than the mould powders and tantalum cannot resists the highly corrosive nature of the fluorine and sodium containing mould slags.

Therefore, an alternative sample holder material was used, a 99% pure nickel containing alloy (Ni 201), because it has a high enough melting point, and nickel alloys are widely used in vessels containing fluorine salts because of their corrosion resistance against reactive materials. The 1µm thick Ni foil was formed into the sample holder's shape by cold pressing. Nickel was chosen because it is formable and the S1 mould powder does not contain nickel, therefore in case of Ni diffusion, the source is known. Nickel also has a relative low diffusion rate in most materials due to its atomic radii which is greater than most elements' in the mould slags, thus it is less likely to affect mould slag solidification through its atomic diffusion. Appendix 1: , contains additional information about the material selection.

3. Experiments

The experimental plan was designed to mimic the mould powder's working environment during the casting process. For all experiments the mould powder was placed in a sample holder. The sample holder was a 2 mm tall cylinder with an 8 mm diameter. Approximately 0,001 gram of mould powder was used for each measurement. The samples were placed in the tempered measurement cell of the Raman microscope. From the initial room temperature (RT1) they were heated to 1200℃ where they were held for the holding time (t_h). After the complete melting and homogenisation of the mould slag, it was cooled to the isothermal holding temperature (T_x). The samples were held there for 1 hour while the spectroscopy measurements were performed at the measurement times (t_n). After1 hour the samples were cooled down to room temperature again (RT2). The complete heat cycle is depicted in Figure 12.

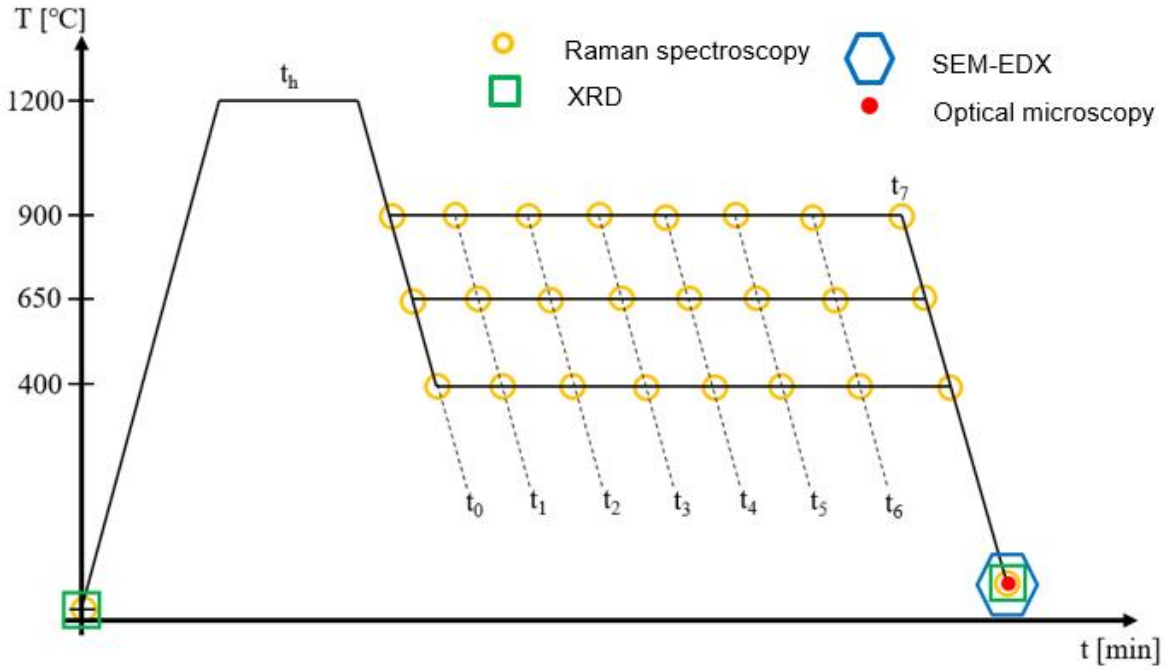

Figure 12 The experimental heat cycle plan with measurement points and characterisation techniques

Table 5 Heat treatment and Raman measurement specifications

$T_{x℃}$ [℃]	400, 650, 900
t_h [min]	5
t_n [min]	0, 4, 8, 16, 30, 60

The melting and solidification took place in the Ni sample holder where the same 20 point positions where measured. The t0 measurements were started when the measurement cell reached the required temperature therefore the absolute time between the 1200˚C and the t0, t1, t2 etc. measurements slightly varied. The maximum heating and cooling speed of the measurement cell, of 200˚C/min was used for all experiments.

Several different characterisation methods were used before, during and after the heat cycle to study the structure of the mould slags. The literature review of the topic that preceded the experiments, identified four structural features that determine the heat transfer properties of

mould slags. The two major factors (phase type, phase ratio) were measured at operating temperatures by Raman spectroscopy. The accuracy of this new method was assessed by a RT2 comparison with the traditional X-Ray diffraction method. The two minor factors (crystal morphology, transition metal oxide distribution) were studied at RT2 by optical microscopy (OM) and SEM-EDX respectively. The time and temperature values of the experimental program are summarised in Table 5.

3.1. Raman Spectroscopy

3.1.1. Sample preparation

The mould powder samples that were used for this research were directly collected from the continuous casting machine's mould powder holders. This way the examined powders were completely representative of the ones used in the process. The powder samples were kept in an airtight container to avoid water pickup after sample collection.

Before heating, the mould powders were crushed and mixed thoroughly to homogenise the multi-component powders and speed up the melting and homogenisation process during melting.

3.1.2. Raman spectroscopy

The Raman spectroscopy measurements were carried out using an inVia™ InSpect confocal Raman microscope manufactured by Renishaw® (Figure 13) [33].



Figure 13 InSpect confocal Raman microscope [33]

The instrument is equipped with two lasers. For most of the experiments the green laser with a 532 [nm] wavelength, was chosen over the red, 785 [nm] one. The lasers vary in laser power. A stronger laser provides a stronger Raman effect, but the drawback of using high laser power is that it can burn the sample. The samples examined in this research were stable structures,

not substantially affected by the laser, therefore a 100% laser power was used in case of the 532 [nm] laser. The green and red lasers have a nominal output of 50mW and 300mW, respectively. The nominal output continuously decreases through the lifetime of the equipment therefore the 100% laser power with the green laser stands for a ~40mW experimentally applied laser power.

The three isothermal holding temperatures were chosen to be 400 ℃, 650 ℃ and 900 ℃ because previous studies [14] have suggested that conventional fluorine-based mould slags have a TTT curve with a nose or earliest crystallisation starting point roughly at 600-700 ℃, plus these temperatures evenly cover the mould powder's working temperature range.

In order to determine the appropriate holding time, two approaches were used. The first, practical approach suggested a 5 min holding time because during normal continuous casting operations the mould slag spends approximately 5 min on top of the liquid steel in the open-air atmosphere before entering the mould – strand gap. The second approach suggested a shorter holding time of 0.5-5 min, because previous mould powder research [32] has shown that these shorter times are sufficient to achieve a homogeneous, gas bubble free melt. As no previous high temperature, melting and solidifying experiments were known with the examined chemistries, two preliminary experiments were carried out to determine the right holding time. During these experiments a RT1-1200-RT2 temperature program was carried out with a 5 min and with a 10 min holding time. The RT2 Raman spectroscopy measurements were almost identical in both cases, therefore full homogenisation was achieved with both holding times. To limit the oxidation and therefore the damage to the sample holder crucible the 5 min holding time was chosen for the experiments.

The measurement times (t_n) were chosen to be 0, 4, 8, 16, 30, and 60 minutes after the measurement cell reached the desired temperature. These points were arbitrarily chosen as in Peterson et. al.'s experiments [14] to cover the same time span. By covering the same time span, the results can be compared to the ones which were obtained by a different method.

A Linkam® temperature and environment cell was used for the temperature program. The cell was connected to a water-cooling unit. This environment cell is capable to maintain temperatures up to 1500 ℃ and have any atmosphere which the accompanying pipeline system supports. For this research a 23-1200℃ temperature range was used with air and argon (Ag) atmospheres. Each temperature program was split into two parts atmosphere-wise. In the first half, when the heating and 1200℃ holding took pace an air atmosphere was used to facilitate and allow the chemical reactions to take place (carbon burn out etc.) similarly to the real-life process. In the second half which consisted of the isothermal holding and cooling to room temperature Argon was used as an atmosphere. This was used to mimic the continuous casting process where the cooling and solidification of the mould slag happens in the strand – mould gap where there is no atmosphere, it is either in contact with the metals or in vacuum [4]. The Argon flow rate was kept at 100 nml/m with a slight deviation due to the gas support system. A high purity (>99%) Ag gas was used for all experiments.

The cooling channels and the induction heating wires were in the base of the sample holder. Temperature control was done by a high precision thermocouple placed at the bottom of the sample holder. The gases flowed in and out at the two sides of the chamber. The AlO glass cover of the chamber was transparent, but it weakened the backscattered Raman signal, therefore it was taken off for the room temperature measurements, where it is not needed.

Several measurement parameters can be modified to achieve the strongest, most clear signal possible. During the experimental trial phase of this research, several setups were explored because there is no universally applicable setup. The experimental trials concluded that two different measurement setups are needed for the room and high temperature measurements with the 532 [nm] laser. This is because the AlO glass cover of the reaction cell weakens the signal, and the Raman signal of high temperature samples is weaker, thus longer acquisition time is needed in the high temperature cases. These two setups are summarised in Table 6.

Other less influential measurement parameters (room humidity, room temperature, Ag gas flow etc.) together with the deviations, if present, from the goal measurement setup are summarised in Appendix 1: Raman spectroscopy measurement details.

Table 6 Raman spectroscopy measurement setup

Laser wavelength [nm]	532		785
Measurement temperature [˚C]	25	400-900	25
Acquisition time [s]	1	10	0.5
Number of accumulations [-]	1	1	1
Grating type [lines/mm]	1200, (2400)	1200	1200
Grating midpoint [cm^{-1}]	1510, extended	1510, 2600, 4600, 5000	1510, extended
Number of measurement points [-]	400-500	20	20
Measurement point spacing [µm]	5-10	20-30	20-30
Objective	50L	50L	50L

At each holding temperature three separate experiment were carried out to account for experimental variability. The 532 [nm] laser in combination with the 50L objective had an approximately 1,3 [µm] spot size.

In the high temperature cases 20 points at the surface of the sample were measured at each time-temperature combination. These points were collected from a 5x4 point grid with a spacing of 20-30µm. At room temperature, the reaction cell was opened and more detailed maps, of 400-500 points were measured with a spacing of 5-10µm. The 532 [nm] laser provided a more detailed Raman spectrum at room temperatures therefore this laser was used for the high temperature measurements.

3.1.3. Optical microscopy

The Raman spectrometer that was used for the research is also equipped with an optical microscope. This optical microscope uses the same optical setup as the laser; therefore, all optical images were taken with the use of the 50L objective. The L in the objective name stands for long range.

The optical microscope is equipped with a digital camera. During the preliminary experiments an optical video was taken from the melting process to verify the melting temperature of the mould powders.

3.1.4. Calculation methods

WiRE™ [34] and Spectragryph [35] programs were used for the spectral analysis. Spectragryph was used for the phase ratio determination, and WiRE for all other analysis.

The crystalline ratio was calculated by three different methods from the obtained Raman spectra. In the first two methods each spectrum (which belongs to a specific point of the sample) was labelled amorphous or crystalline. After the labelling the crystalline to amorphous ratio was determined as the number of crystalline points divided by the number of all measurement points. The labelling was done in both calculation cases by comparing two characteristic peaks. In calculation method 1 the characteristic peak's height (intensity), in calculation method 2 the characteristic peak's area was used to quantify the peak. After the quantification the two numbers were compared, and the higher number's label was assigned to the point. The 911 [cm^{-1}] characteristic peak was used as the representative crystalline peak, because it belongs to the Si-O stretching vibration when the Si tetrahedron has 1 bridging and 3 non bridging oxygen atoms. The 563 [cm^{-1}] characteristic peak was used as the representative amorphous peak, because it belongs to the Al-O stretching vibration. Al atoms are not part of the crystalline structure thus they are present in the amorphous phase [31]. One measurement point can contain both crystalline and amorphous phases which results in an error in this calculation method that was partially reduced with the increase in the number of measurement points, but even with 5000 plus measurement points these calculation methods were not as accurate as the following one, due to the assumption made during the labelling.

The third calculation method utilises the Spectragryph program's built-in phase ratio calculator. This calculator uses the Raman spectra of the pure components to determine the phase ratios through a multi linear regression (MLR) calculation. Raman spectra are only available for cuspidine in the literature, not for combeite which is the other crystalline phase, thus no pure spectra could be used for the crystalline ratio calculations. To overcome this knowledge gap two spectra from the experimentally acquired ones was used as the input for the MLR calculation. For the crystalline phase the E2-m15/2453 (experiment number-measurement number / measured point number) spectra, for the amorphous phase the E2-m15/219 spectra were used. Because both spectra are mixed spectra, they were not collected from pure samples, the accuracy of this calculation method is lower than what can be achieved with pure spectra, but synthetising pure cuspidine, combeite and amorphous samples was out of scope for this research.

3.2. X-Ray Diffraction

The X-ray diffraction (XRD) measurements were performed according to Tata Steel Netherland's internal standards. This consists of the two steps of the measurement and the post processing.

All XRD measurements were performed using a fully automated Bruker D8 Endeavour diffractometer equipped with an energy sensitive strip detector (Lynxeye XET). Radiation used was CoKα (wavelength: λ = 0,1789 nm). Data were collected in the range of 10° to 100° 2Θ with a step-size of 0.02°. Total collection time was 60 minutes. Data processing was done using the Bruker Diffrac.EVA (Phase ID) and Bruker Diffrac.Topas (Quantification Rietveld approach).

The mould slag samples were examined with XRD after the heat cycle and Raman measurements. The slag samples were removed from the sample holder crucibles and ground with a mortar. The slightly grounded mould slag samples were mounted on a zero-background silicon wafer holder in the XRD machine.

3.3. Scanning Electron Microscopy

Scanning electron microscopy (SEM) measurements were made with a Zeiss Gemini SEM 450. Images were collected with both the SE and BSE modes to acquire topology and chemical composition maps. The samples were not coated with a conductive material which resulted in sample charging in some areas.

3.4. Thermodynamic calculations

The phase fraction calculations were performed with the FactSage 8.1 software. The CON4 database was used for the calculations which is optimised for solution phases and especially slags. The nominal composition, that is depicted in Table 2 was used as the starting composition with air as an atmosphere. The phases at equilibrium and phase fractions were calculated up to 1400℃.

4. Results

4.1. Raman Spectroscopy

4.1.1. Room temperature results

After the heat treatments the samples were studied with both the 785 [nm] and the 532 [nm] laser. Examples of the acquired spectra are shown in Figure 14 and Figure 15 respectively. At room temperature the different spectra were measured at different positions on the sample surface. In case of the 785 [nm] laser, independent of the position, the same type of spectrum was collected. From position to position only the measured peak's relative intensity varied.

The Raman spectrum measured with the 785 [nm] laser was screened through the available databases, to find the measured material. In the RRUFF database a match was found. The measured spectrum was a match with the cuspidine spectrum of the database [37]. The 100-2200 [cm^{-1}] part of the measurement and database spectra are shown in Figure 14. The two spectra contain similar peaks with a consistent 75 [cm^{-1}] peak position shift which is the result of the different excitation wavelength.

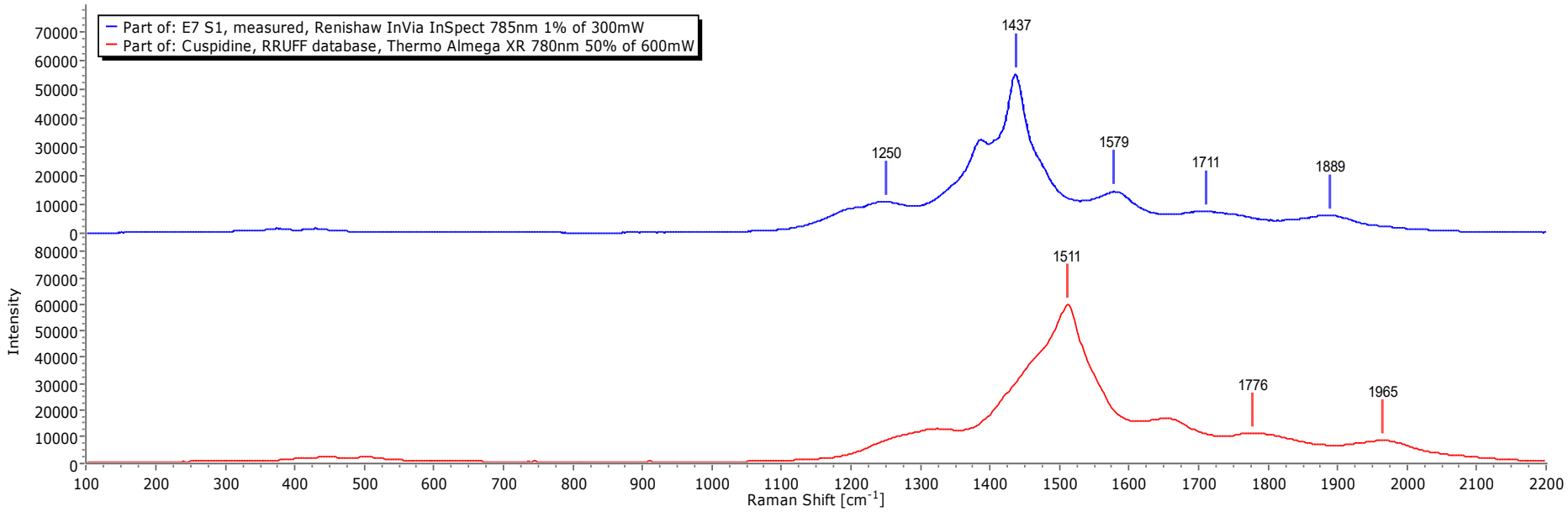

Figure 14 Raman spectrum measured with the 785 nm laser compared with the RRUFF database Raman spectrum of cuspidine measured with a 780nm laser [37]

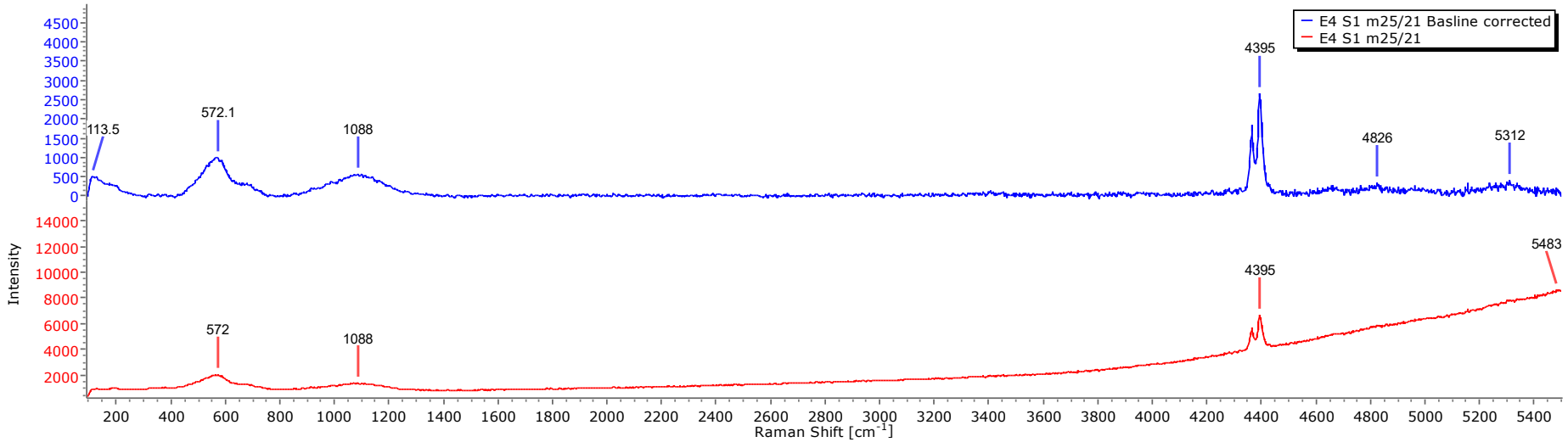

Figure 15 Measured Raman spectra type 1 examples: raw and baseline corrected spectra of E4 m25/21

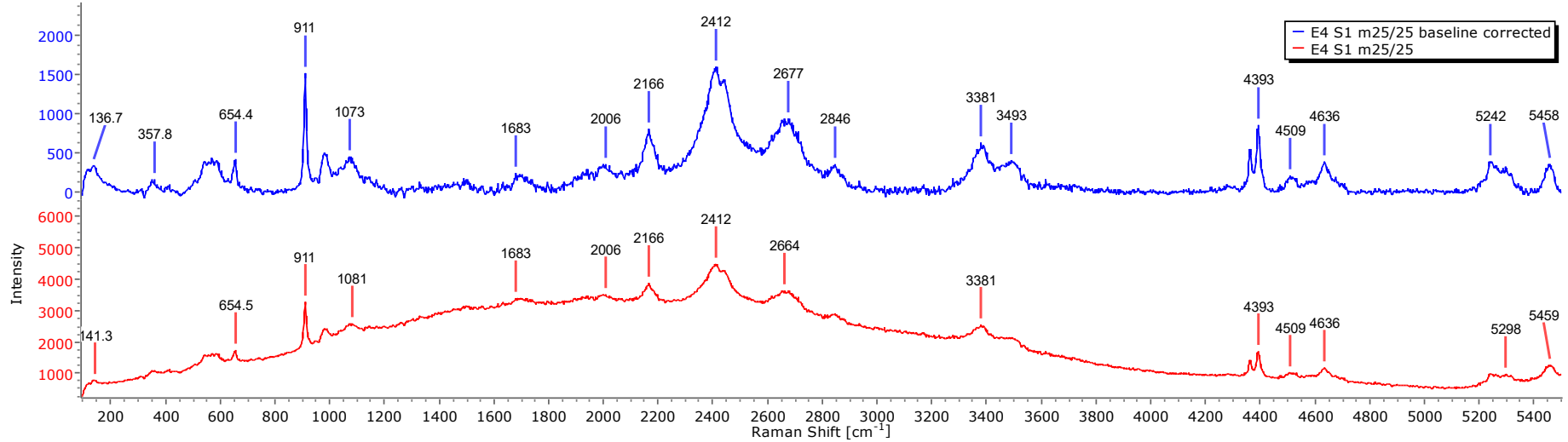

Figure 16 Measured Raman spectra type 2 examples: raw and baseline corrected spectra of E4 m25/25

With the use of the 532nm laser two distinct type of spectra were observed at room temperature. An example of type 1 is depicted in Figure 15, while an example of type 2 in Figure 16. Type 2 spectra had a large peak by peak intensity variation, which means that those spectra are the result of two or more components in the measured area. The variation in the peak-by-peak intensity is due to the ratio variation of the phases in the measurement area. In Raman spectroscopy the peaks on the intensity – Raman shift diagram is the result of a certain type of atomic bond vibration; therefore, they are representative of a specific bond. To identify, understand and then finally follow the structure change of materials first the observed peaks are identified.

4.1.1.1 Raman peak identification

More than 20 different peaks were observed in the Raman spectra in the wavelength range of 100 – 5000 [cm^{-1}]. Because the observed crystalline spectra have changing relative peak intensities this means that these spectra contain at least two different components and the relative peak height fluctuations are caused by the mixture ratio change. Therefore, the examined S1 mould slag has at least three different phases, with one being an amorphous phase (type 1). One of the crystalline phases is cuspidine as identified by the 780 nm laser measurements.

The type 2 crystalline spectrum had no acceptable matches from the Raman databases used (RRUFF, Rhenishaw) therefore the crystalline phase(s) other than cuspidine cannot be identified.

To gain a deeper understanding about the type 2 spectra the individual peaks were examined. Mould slag characterisation by RS is a relatively new field therefore due to the gaps in current knowledge, not all peaks could be assigned to a certain vibration, in spite of the extensive literature and database searches carried out through this thesis. Five peak areas could be identified with certainty based on previous research, the other areas and the possible explanations are discussed in more detail in Appendix 3: Raman spectrum band assignment proposals.

Research [38, 39] has identified the 430-600 [cm^{-1}] wavelength range as the Al-O stretching vibration in the AlO_4 tetrahedron. The examined mould powders often showed a 563 [cm^{-1}] peak, especially in case of the type 1 Raman spectra. This peak belongs to the Al-O stretching vibration. Depending on the number of bridging oxygen atoms in the tetrahedrons, the peak position of the network forming tetrahedrons can shift. The measured average peak position of 563±6 [cm^{-1}] of the Al-O vibration means that the aluminium tends to form more complex structures than monomers by having more bridging oxygen atoms than non-bridging ones in the tetrahedrons.

The 654±1 [cm^{-1}] peaks belong to the Si – O bending vibrations. This peak was previously reported on several slag research [40]. This peak, like other Raman peaks become sharper as the Si-O structure become more ordered.

In the range of 850-1150 [cm^{-1}] there can be four peaks that belong to silicon-based structures. These four peaks are located at 870 [cm^{-1}], 911 [cm^{-1}], 975 [cm^{-1}], and 1070 [cm^{-1}]. All four peaks correspond to the Si – O symmetric stretching vibrations. The difference of the four peak positions is caused by the number of O atoms that are bridging or non-bridging in the structure. A bridging oxygen atom is bonded to two Si atoms, thus is part of two tetrahedrons.

The four peaks are the result of 0, 1, 2, or 3 bridging oxygen atoms per tetrahedron. These peaks are commonly denoted by Q^0, Q^1, Q^2, and Q^3 respectively. A Si-O tetrahedron can also have four bridging oxygen atoms, which means that the formed structure is a fully crystalline one. This structure is the quartz structure. The Q^4 Si-O bonds are not Raman active bonds, therefore cannot be detected by Raman spectroscopy measurements [31, 36].

The peaks at 3384±5 [cm^{-1}], and 3496±5 [cm^{-1}] belong to the OH vibrations of H_2O [41, 43, 44]. The origin of the water can be either traced back to the powder form where the mould powder picks water up from the air, or it can be also a result of one of the many chemical reactions when the oxides and hydroxides react during powder melting.

The double peak at 4362±3 [cm^{-1}], 4391±5 [cm^{-1}] is not from the sample material because it is an inherent signal of the machine. Therefore, it should be disregarded.

4.1.2. Results of high temperature measurements

The high temperature structure of the mould slag was studied through Raman spectroscopy measurements at 400°C, 650°C and 900°C. Spectra were collected 0, 4 8, 16, 30 and 60 minutes after reaching the desired isothermal holding temperatures. In general, the high temperature spectra are less clear than the room temperature ones. The difference in between the spectrum qualities is caused by both physical and measurement effects.

With increasing temperature, the thermal radiation component of the Raman signal increases too. This thermal radiation component can be mostly removed in the data processing step by subtracting the baseline of the spectra, but it introduces a larger error in the low wavelength area of the spectra (100-160 [cm^{-1}]). Random fluctuations in the thermal radiation also occur which reduce the quality of the spectra [42].

Measurement-wise there are also two factors that affect the quality of the high temperature Raman spectra. During the high temperature measurements, the samples are enclosed in the experimental cell, and both the excitation laser and the Raman signal goes through an additional glass layer which weakens the signal. More importantly, mould powders and mould slags partially lose their fluorine content. The lost fluorine forms a thin semi-transparent layer on the inner surface of the experimental cell. This layer further decreases the quality of the Raman signal. The fluorine layer formation was minimized by increasing the argon flow rate in the experimental cell, but it could not be completely eliminated. Fluorine loss is a known phenomenon in continuous casting and due to its negative health effects, research is focused on F-free mould slag development.

Both the physical and measurement effects decrease the quality of the Raman spectra at high temperatures therefore the weaker Raman peaks cannot be reliably identified. However, the Q1 peak of the Si-O bond is visible at all temperatures (Figure 17) which makes it possible to partially follow the structure changes related to the Si-O tetrahedron at high temperatures.

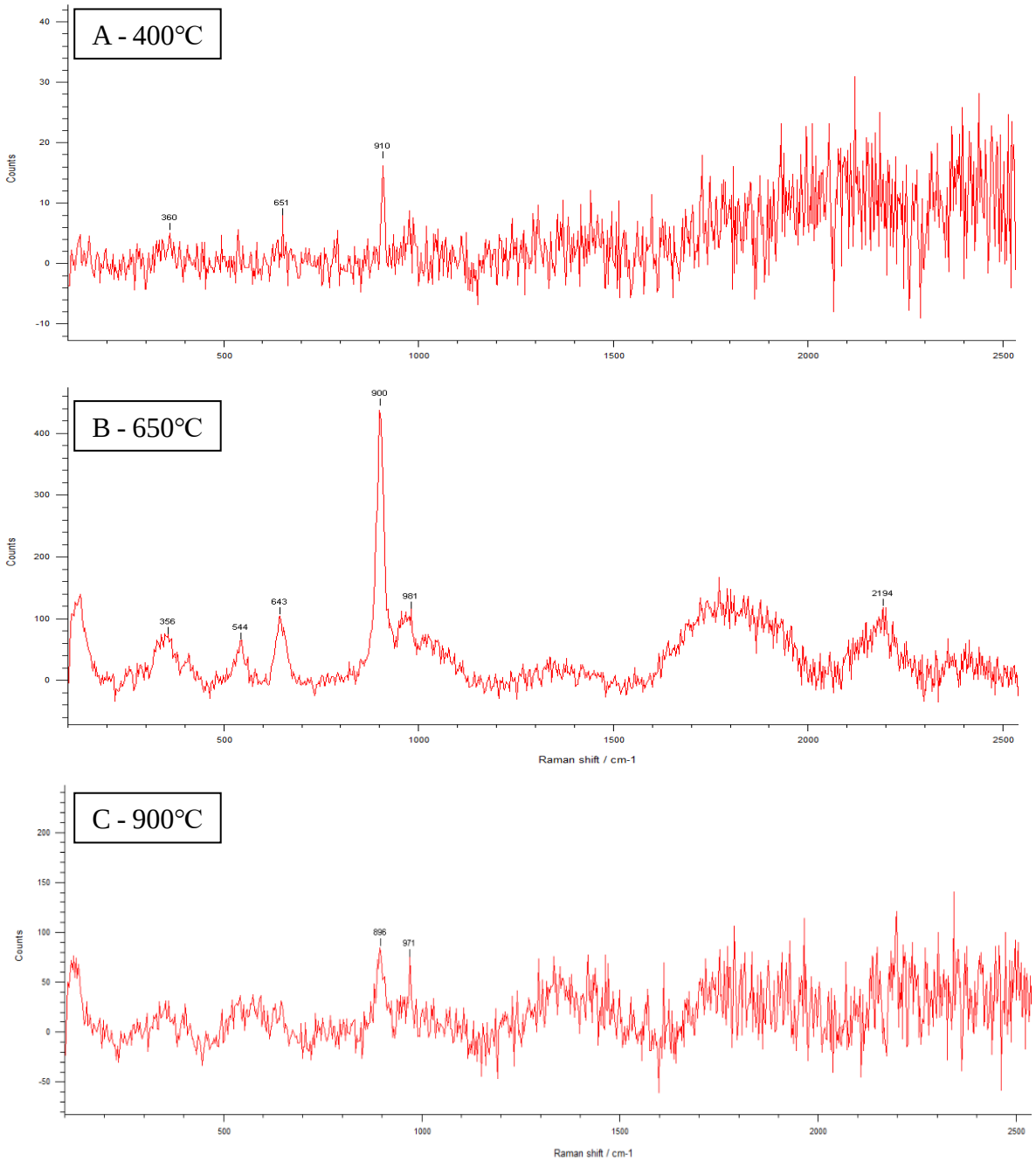

Figure 17 High temperature Raman spectra examples of S1 a: 400°C b:650°C c:900°C

The Raman shift of a given peak steadily decreases with temperature increase. The peak position shift is not universal, each type of bond has its own shifting behaviour. Most of the peaks that are high in intensity and clearly visible at room temperature, like the Q1, Q2, and the Si-O bending bond, is also detectable in the high temperature spectra. The most notable difference is the 2412 [cm^{-1}] peak which is only visible at room temperature (Figure 19). The two spectra in Figure 19 have been taken at the same sample position (although a minimal position shift is always present in all measurements due to dilatation), with the same measurement setup, atmosphere etc. the only difference being the temperature. This makes the two spectra comparable and eliminates most of the measurement differences.

The comparison of the same temperature spectra through time showed no significant changes in spectra type. All samples showed a weakening Raman signal as the experimental time progressed which is due to the thickening of the fluorine layer and the increase of light scattering by it (Figure 18). The 400°C measurement results' accuracy is so low that it was deemed unreliable and was discarded from the discussion. The decrease in the average intensity means that the amount of light that correspond to the given Raman shift decreases with time. The decrease can be either attributed to the weakening of the Raman effect or to an increase in the electromagnetic waves that gets scattered in the space between the CCD collector of the Raman spectroscope and the sample. The Raman effect weakens or strengthens at the Q1 or Q2 wavelength if a phase transition takes places that result in the change in the number of bonds that are responsible for the given Raman shift.

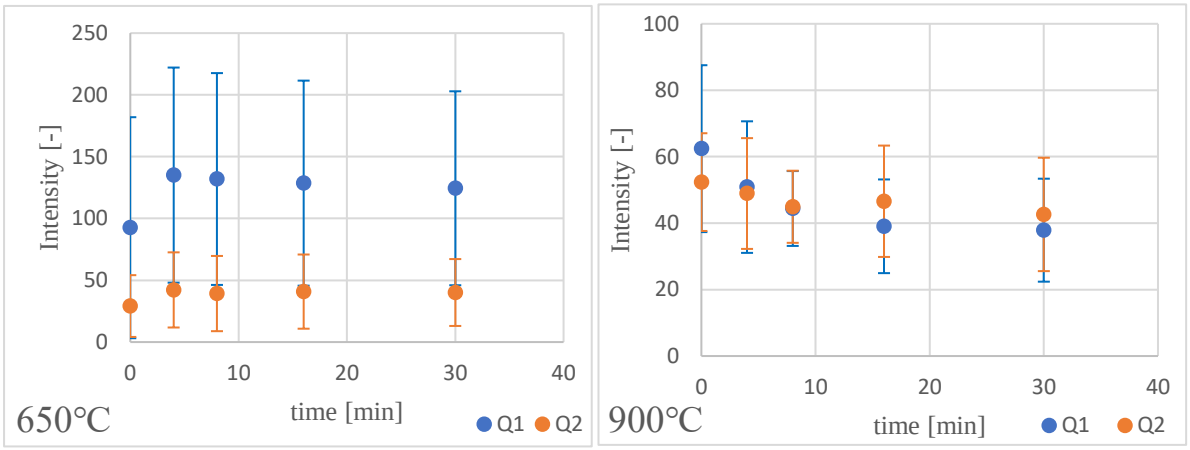

Figure 18 The average peak intensity changes through the heat treatment of the different Si-O Raman bands (Q1, Q2)

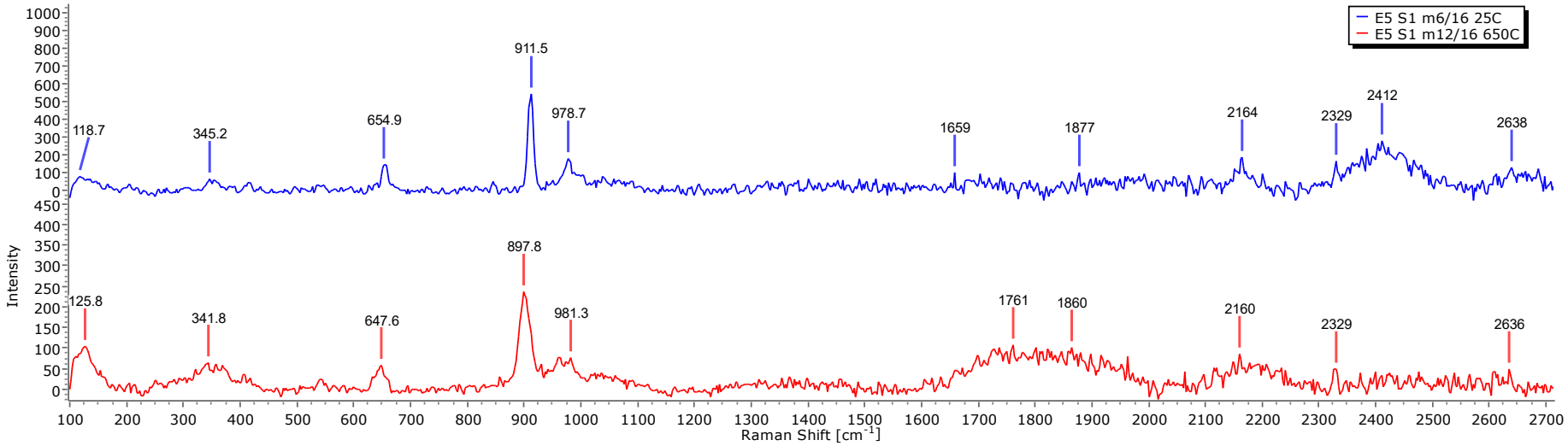

Figure 19 Raman spectrum of the S1 mould slag at 25˚C and 650˚C measured with a closed measurement cell

4.2. X-Ray Diffraction

The XRD measurements identified 4 different crystalline structures in the mould slag samples. These four structures are: cuspidine, combeite, nickel oxide, and nickel metal (Figure 20). Metallic nickel and nickel oxide are not part of the slag structure, they are contaminations on the sample. The mould slag samples could not be measured while still in the sample holder because the sample holder's walls limited the 2Θ angle of the measurement, thus they were taken out from the sample holders. This could be easily done by slightly bending the sample holder, when the rigid mould slag sample became detached from it. Although it easily detached, it still "pulled" the nickel oxide layer and some metallic nickel with it, which was subsequently detected by the XRD.

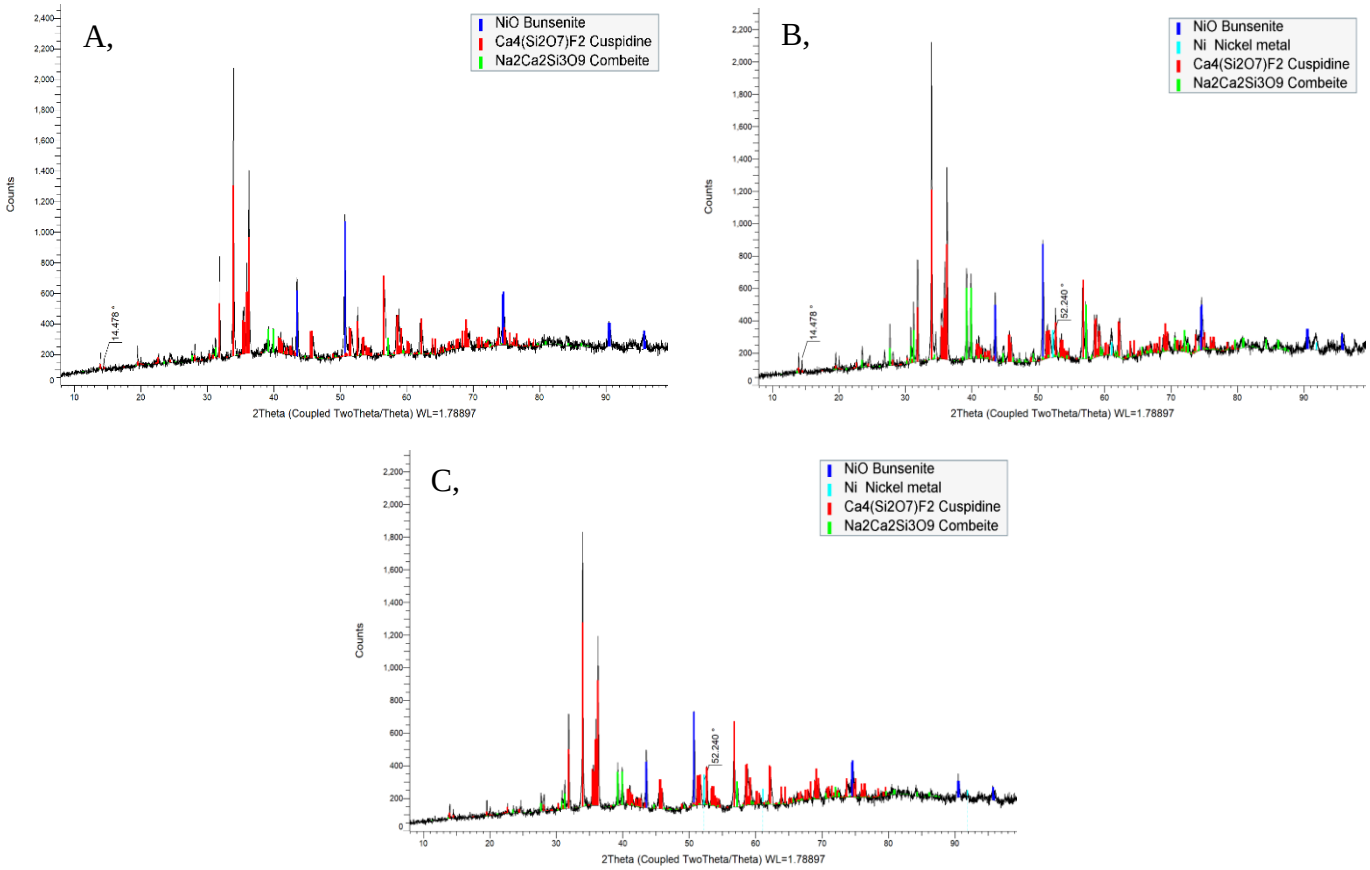

Figure 20 XRD results of the S1 mould slag at room temperature after: A: 400℃, B: 900℃, C: 650℃ heat treatment

Table 7 Rietveld full profile refinement analysis results of the S1 mould slag samples after the 400°C, 650°C, and 900°C heat treatments

	A – 400°C	C – 650°C	B – 900°C
NiO (Bunsenite)	10,44±3%	7.58±2%	7,14±2%
Ni (Nickel metal)	0	0,21±2%	1,27±2%
$Ca_4(Si_2O_7)F_2$ (Cuspidine)	74,95±7%	71,50±6%	63,65±5%
$Na_2Ca_2Si_3O_9$ (Combeite)	14,61±3%	20,71±3%	27,94±4%

The subsequent Rietveld-analysis determined the fraction of each phase (Table 7). The XRD measurements cannot directly detect the presence of the amorphous phase because of the small sample size therefore the results obtained by Rietveld analysis should only be used as a relative value (for example as a combeite to crystalline ratio) and not as an absolute one.

4.3. Scanning electron microscopy

Images were taken in both the secondary electron (SE) and energy dispersive spectroscopy (EDS) mode, from the three different heat treatments. The samples were taken to the SEM from the Raman microscope.

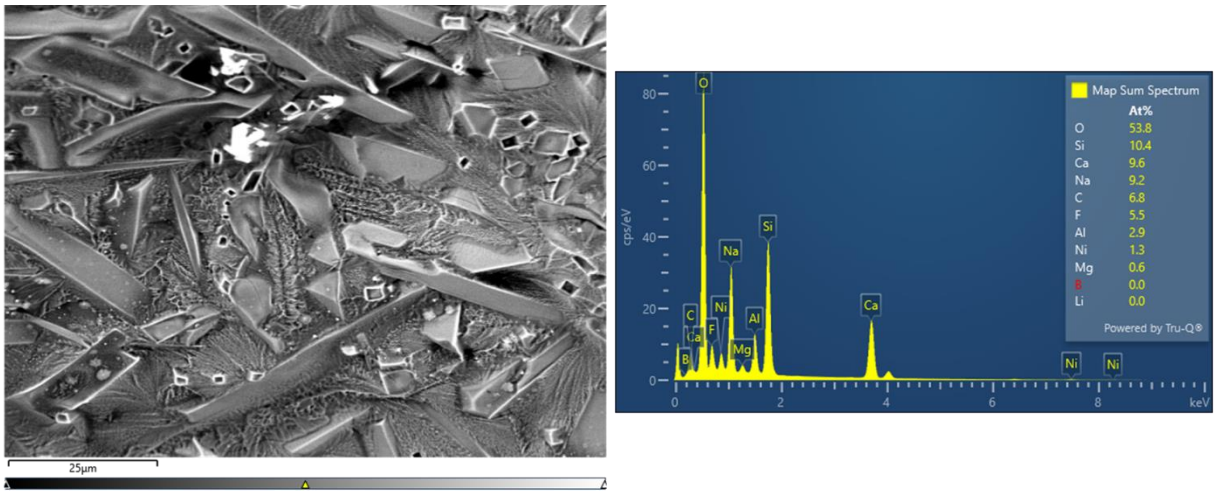

Figure 21 Left: atomic contrast SEM image E2 (650°C), Right: chemical composition of E2 (650°C) measured by SEM

A typical SEM result is depicted in Figure 21. After the conversion from at% to wt% the areas chemical composition is: 3,9 wt% C, 40,9 wt% O, 4,97 wt% F, 10,1 wt% Na, 0,7 wt% Mg, 3,7 wt% Al, 13,9 wt% Si, 18,3 Ca, and 3,6 wt% Ni.

In Figure 22 the elemental distribution of Na, Ni, Al, O, F, Si is depicted. The elemental distribution is in line with the atomic contrast and topology images. These results show that certain elements tend to cluster together forming three chemically different areas. Ni is only present in area 3 together with O, which is present in all three areas. Si and Ca are present in both area 1 and 2. F is mostly present in area 1. Al and Na are present only in area 2.

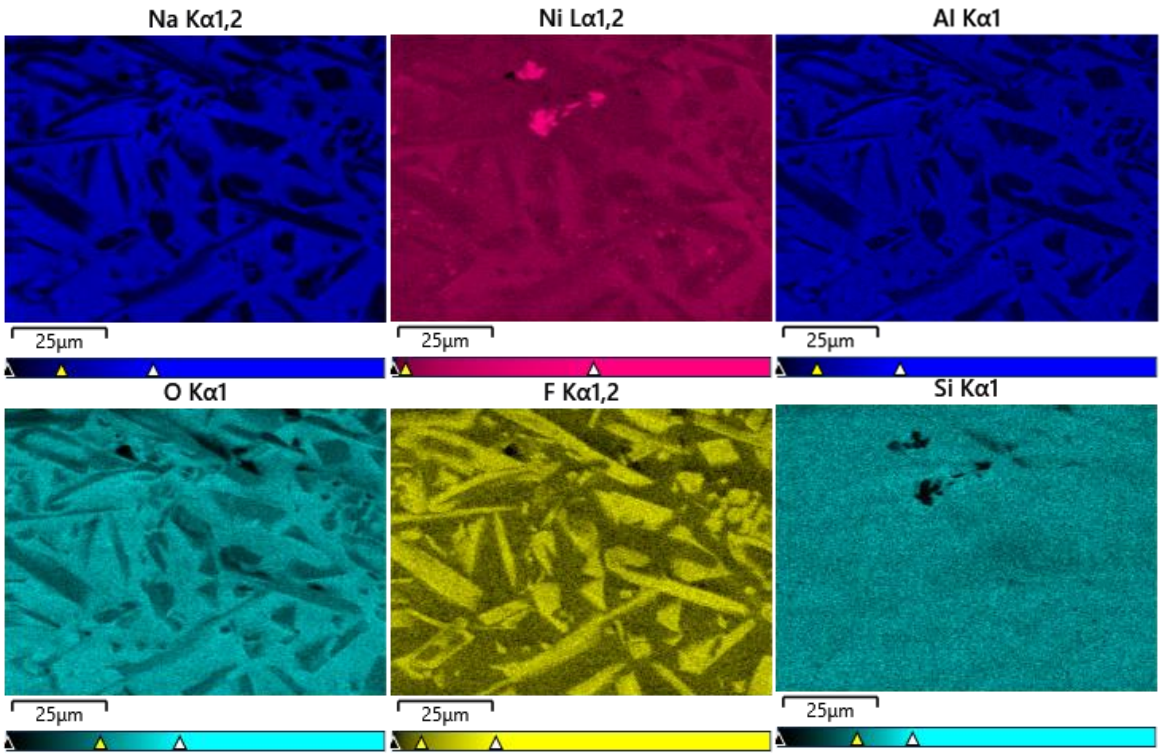

Figure 22 Elemental distribution for selected elements of E2 (650℃) measured with SEM-EDS

The S1 mould slag after solidification has a complex microstructure. It is made of large (~10-30 um long, ~1-10 um thick) faceted crystals (area 1) in a surrounding matrix (area 2). Zooming more into area 2, a high magnification image (Figure 23) reveals that it is not a continuous area but rather made of two, one of which has a dendritic structure.

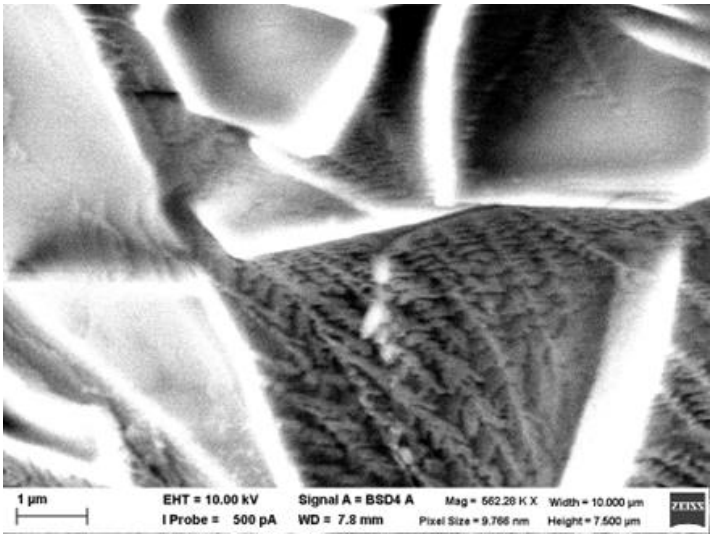

Figure 23 Detailed atomic contrast SEM image of E2 (650℃)

The samples after the other two heat treatments (400 ℃ and 900 ℃) have similar microstructures. The elemental distributions are also similar. The one notable difference between the samples which went through different heat treatments (Figure 24) is the Ni amount and distribution. While the 400 ℃ and 650 ℃ samples have only localised clusters of Ni, the 900 ℃ sample has Ni across the sample. In conclusion, the morphology is the same

for all the different heat treatment temperatures, as are the elemental composition and distribution with the exception of Ni in case of the 900 ℃ sample.

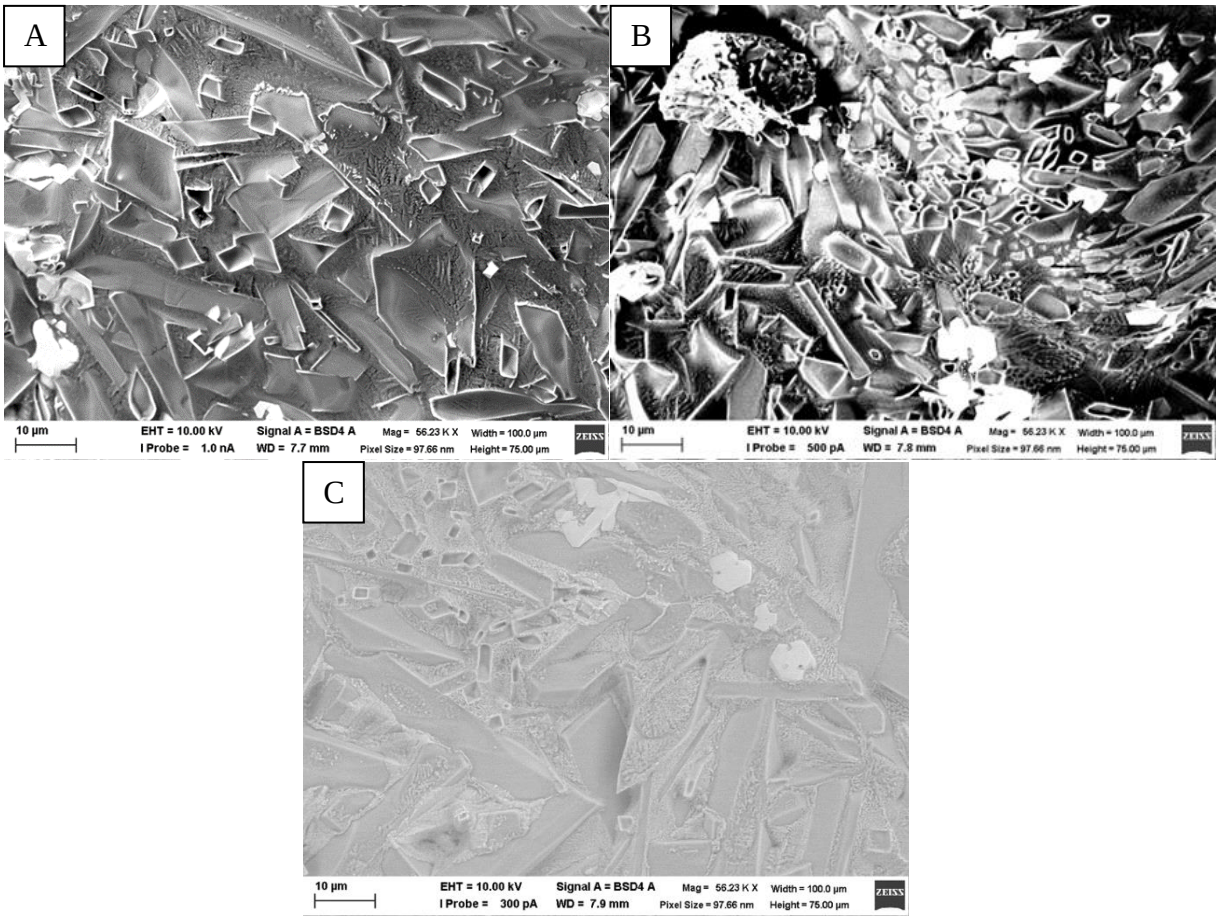

Figure 24 SEM atomic contrast images of the microstructure of the S1 mould slag after heat treatments at A: 400℃, B: 650℃, C: 900℃ temperatures

The overall crystalline ratio measured and calculated by the different methods are shown in Table 8. In the thermodynamic calculation, all remaining liquid slag was assumed to form an amorphous phase. In the SEM based estimation the overall area of the cuspidine plus combeite was calculated.

Table 8 Overall crystalline ratio results by the different characterisation methods

Characterisation method	Raman spectroscopy			SEM-EDS	XRD	Thermodynamic calculation
Calculation method	M1: Peak	M2: Area	M3: MLR	ImageJ (estimate)	Rietveld analysis	FactSage
400℃	86±10%	83±13%	77±8%	79±5%	100%	100%
650℃	92±7%	90±10%	81±11%	80±7%	100%	100%
900℃	89±5%	86±5%	73±6%	-	100%	80%

4.4. Thermodynamic calculations

With the use of FactSage the S1 mould slag's phase types and phase fractions has been calculated in the temperature range of 400-1400°C. The results are shown in Figure 25. Only phases above 3 weight % are drawn in the figure, the others were discarded. The calculation has shown that a solid crystalline phase (cuspidine) can be present up to 1300°C. The other major crystalline phase, combeite is only present in measurable quantities at temperatures lower than 1100°C.

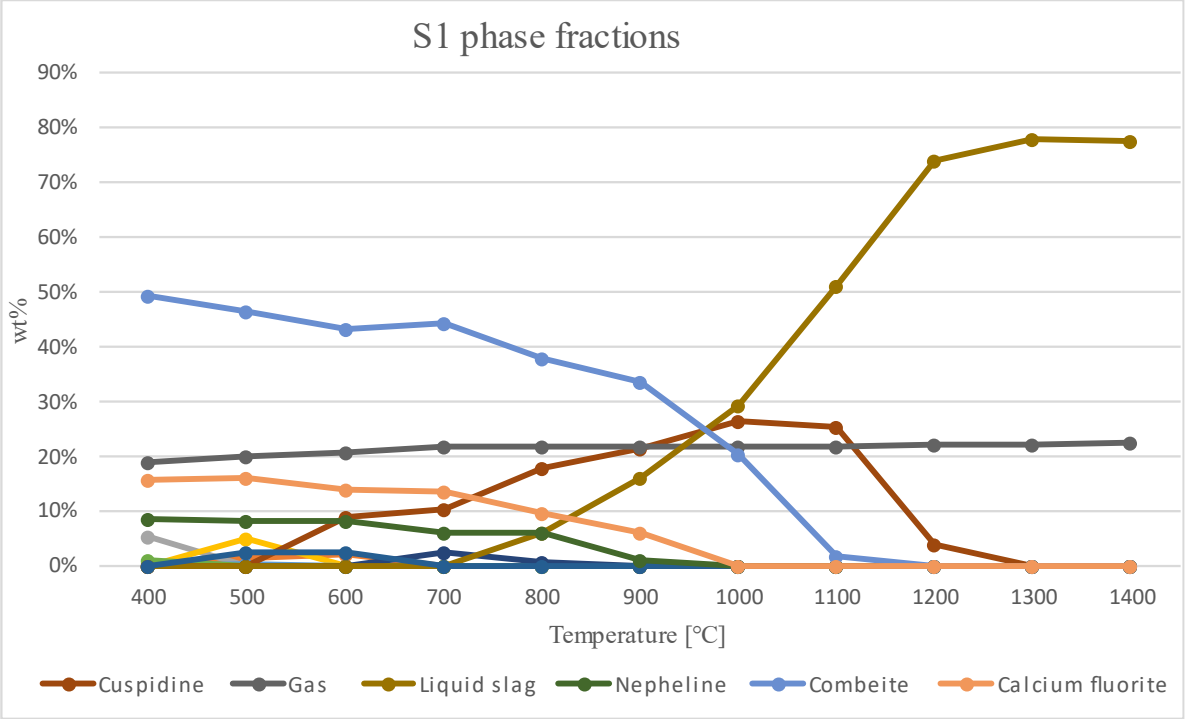

Figure 25 The phases and phase fractions predicted by thermodynamic calculations of the S1 mould slag at different temperatures

The numeric results of the cuspidine and combeite phase fractions at the three high temperature Raman measurements are shown in Table 9. These results indicate that cuspidine is not an equilibrium phase at 400°C, and the cuspidine to cuspidine to combeite ratio increases with temperature. Combeite is present in larger amount than cuspidine at all three temperatures. This is true until 900-1000°C when it switches to the other way around. Cuspidine is more stable at temperatures above 1000°C than any other crystalline phase.

Table 9 Calculated cuspidine and combeite phase fractions of S1 mould slag at high temperatures

	900°C	650°C	400°C
Cuspidine [wt%]	0,2464	0,1116	0
Combeite [wt%]	0,3895	0,5061	0,572
Cusp/comb [-]	0.63	0.22	0

5. Discussion

The aim of this research has been to measure and understand the slag structure and formation of the S1 mould powder with a special focus on the physical properties that determine its heat transfer behaviour.

During all heat treatments a limited fluorine and sodium loss was observed as sodium-fluorine formed on the experimental cell walls. To account for this loss the mould powders target composition (Table 2) was compared with the composition measured by the SEM after the heat cycle (Figure 21). Although the accuracy of this comparison is not perfect due to the SEM-EDS characterisation method's varying sensitivity to different elements, and possible surface to bulk correlation issues, in most cases the measured values were not deviating largely from the target composition. F, Na, Al, and Ni were the only measured elements that deviated from the nominal composition. F and Na was lost through the heating cycle, which mimics the actual continuous casting process where F loss is also observed therefore this doesn't decrease the results applicability to the real-life process. Ni originated from the sample holder not from the material therefore it can be disregarded. During the experiments the sample was not in contact with any Al source therefore the Al content of the measured sample was originally higher than the target content set by the manufacturer. This can be the reason of an unknown recipe change or a variability in the source minerals which caused the change.

5.1. Structure of the mould slags

5.1.1. Room temperature structure

With the use of the 785 [nm] laser, only the cuspidine structure was collected, independent of the measurement point position. This would suggest that the structure of the mould slag is a simple one phase structure, which is not the case because other phases are present too. The 785 [nm] laser only measured the cuspidine phase because its lateral resolution is much worse than the 532nm's or the SEM's and also different bonds have different Raman scattering if the excitation wavelength is changed. This means that the measurement area is so large, in case of the 785 [nm] laser, that a cuspidine phase will always be present in the measured area, and or this specific wavelength is not sensitive to the other phases. The cuspidine structure's Raman signal is the strongest of all the present phases, therefore that will be dominant at all measurement points. In view of the bad spatial resolution in combination with the strong cuspidine signal, the in-depth analysis of the mould slag structure was mainly through the Raman spectra collected with the 532 [nm] laser.

5.1.1.1. Phase types

At room temperature (25 °C) the S1 mould slag has a multi phased structure with complex morphology. It consists of three major phases. Out of these three, two were confirmed by XRD to be crystalline. These two crystalline phases are cuspidine and combeite. The third phase is an amorphous Si-glass. A fourth phase was also detected in small amount by the SEM measurements (Figure 22), with it being NiO from the sample holder. The change of the isothermal holding temperature did not affect the phase types that were formed during the experiments.

The crystalline phases, cuspidine and combeite were not detected as two distinct phases in the Raman microscopy measurements (Figure 26). This is because combeite is a rare mineral, no Raman spectra is available of the phase therefore it's spectrum could not be separated from the acquired spectra which was acquired from spots of more than one phase.

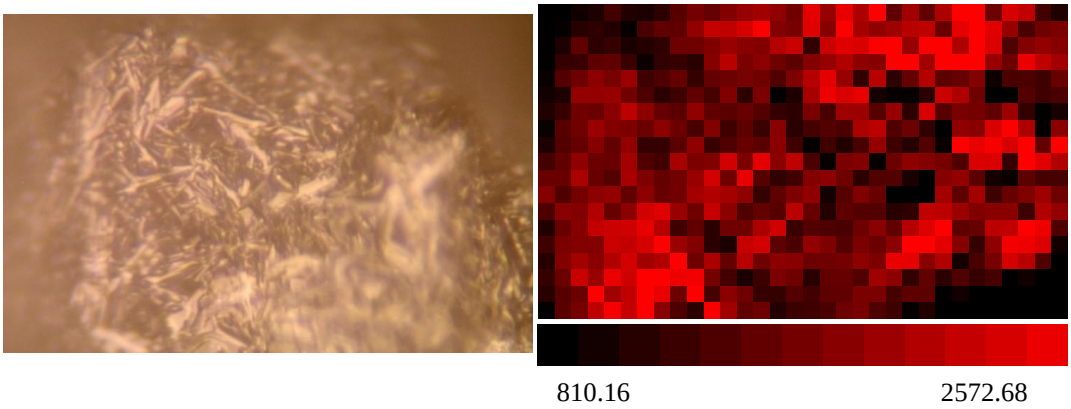

Figure 26 Left: optical image Right: Raman intensity at 911 [cm-1] (Q1 peak of Si-O) of E5 at room temperature

The Si tetrahedrons have different number of bridging Oxygen atoms in cuspidine and combeite. In cuspidine the Si tetrahedrons contain 1 bridging O atom thus a Q1 peak is strong and pronounced in this structure at 911 [cm^{-1}]. In the Combeite structure Si tetrahedrons contain 2 bridging O atoms thus in this structure the Q2 Raman peak will be more pronounced at 965 [cm^{-1}]. Although this difference is there in their theoretical Raman spectra, the experimental results cannot be accurately separated to cuspidine and combeite spectra purely based upon this because both structures can be distorted which will lead to different Si-O bandings and thus different Q peaks showing up in the Raman spectra. Therefore, to perform accurate phase identification a detailed Raman spectrum is needed of the possible pure mould slag phases.

The XRD results (Figure 20) confirmed that cuspidine is not the only crystalline phase in the sample but combeite is also present. The XRD measurements showed the presence of Nickel and nickel oxide too in the sample. These two phases are not part of the mould slag structure. The nickel and nickel oxide contamination happened during sample transportation and XRD sample preparation. Both these phases originated from the sample holder and are not part of the mould slag in continuous casting operations.

The thermodynamic calculations (Figure 25) predicted the formation of other phases too like nepheline or calcium fluorine. Although several samples were kept at an isothermal holding temperature of 900℃ for 1 hour, this time was not enough to form these phases due to the kinetic barrier. Another explanation for the absence of the other phases are the inaccuracies of the calculation. The calculation assumes that all constituents are in form of oxides which is widely assumed in mould slag research, but possibly untrue. The other false assumption made in the calculation is the composition. Mould powders are made of open pit mined minerals thus their chemistry is subject to large deviations from the nominal one. This deviation was confirmed by XPS in case of the S1 mould powder (Figure 35). The XPS results (Appendix 5: X-ray photoelectron spectroscopy results) confirmed that the S1 sample contains also boron, which can affect the thermodynamics of the slag system and thus the

final phase types too. Therefore, the difference between the measured and theoretically calculated phase types is the result of the combined effect of the phase formation speed (kinetics) and the incorrect calculation assumptions.

5.1.1.2. Phase ratios

The phase ratios were calculated from the results of RS, XRD, the thermodynamic phase fraction calculations and approximated from the SEM-EDS results. The RS results were interpreted three different ways as there is no standardised method how to calculate the phase fractions from a detailed Raman mapping image. Due to the lack of a pure combeite Raman spectrum, the cuspidine to combeite ratio could not be determined, only the overall crystalline ratio, from the Raman results. Out of the three proposed calculation methods, the third, multi linear regression-based method was the most accurate.

In order to get a comparison for the crystalline to amorphous ratio based on the Raman measurements, a rough approximation was carried out from the SEM results. In this approximation, it was assumed that the areas with high F content correspond to the cuspidine crystals area (yellow area in Figure 23), the dendritic crystals area correspond to the combeite crystals area and the remaining, Al containing area is the area of the amorphous phase. The crystalline to amorphous ratio was calculated from these three areas. This estimation reviled that the 400°C, 650°C, and 900°C samples had a cuspidine area fraction of 51.5±2%, 43.7±8%, and 55.8±4% respectively. The combeite area fraction could only be determined for the 400°C, 650°C cases because the Ni diffusion made the high magnification images uninterpretable in case of the 900°C cases. The 400°C, and 650°C samples contained 28.2±2% and 36.1±5% combeite respectively.

The XRD measurements did not detect the amorphous phase due to the small sample size and low amorphous to crystalline ratio, therefore it showed a 100% crystalline structure for all cases. This limitation can be overcome by increasing the sample size, but that would require an additional melting and solidifying step because the sample size was almost at a maximum which the reaction cell used in this study can handle.

The thermodynamic calculations were interpreted in a way that at each temperature the liquid slag was treated as the amorphous phase, and the overall crystalline ratio was calculated accordingly. The results of the calculations are summarised in Table 10.

Table 10 Phase fractions, at the three experimentally examined temperatures, according to the thermodynamical calculations

	cuspidine	combeite	slag	CaF	nepheline	$CaCO_3$
400°C	0.0%	49.8%	0.0%	15.9%	8.7%	5.3%
650°C	8.3%	42.7%	0.0%	14.2%	9.5%	0.0%
900°C	21.3%	33.7%	16.0%	6.1%	1.0%	0.0%

Comparing the overall crystallinity results across the different characterisation and calculation methods (Table 8) it is obvious that the first two calculation methods of the RS calculations perform poorly, therefore should not be used. This is due to the methods assumptions, because it fails to account for the mixture of phases in a single Raman measurement

The multi linear regression-based method's results are in the measurement error range of the SEM approximation results which proves the validity of this method in determining the crystalline ratio of mould slags. Although the method is promising, the high level of uncertainty of the results (it can be as high as ±11%) shows that further improvement is needed to make this method widely applicable.

In conclusion, the experimental results showed that cuspidine was the main crystalline phase in the mould slags in all cases. Combeite was the minor crystalline phase with and the amorphous glass phase being the third one.

5.1.1.3. Transition metal oxides

Nickel oxide was the only transition metal oxide that was detected through the experiments. It was detected in the SEM and XRD measurements, not in the Raman spectroscopy measurements. This is because NiO originated from the sample holder cup and not from the mould slag thus it is only detectable after the sample transportation from the Raman experimental cell to the other machines.

Discarding the NiO, the S1 mould powder does not contain transition metal oxides as a separate phase. This was expected based upon the starting chemistry because no transitional metal is listed except iron (Fe) which is only included in small quantities.

5.1.1.4. Morphology

Regardless of the heat treatment the samples had a similar morphology. The samples consist of large faceted cuspidine crystals which are in a matrix of small dendritic combeite crystals and amorphous glass. The shape and size of the cuspidine crystals were similar in all three cases (Figure 24).

5.1.2. High temperature structure

The high temperature structure of the mould slag was directly observed by Raman spectroscopy. The acquired results (Figure 17) showed high level of similarity to the room temperature spectra (Figure 19). The spectrum quality and the peak positions are two differences in the spectra. The presence of the same peaks, although with slightly shifted peak positions, means that the same bonds are present in the material at all temperatures. The same bonds are present at all examined temperatures indicating that the overall structure of the mould slag is made of the same phases.

At high temperatures the peak position of the measured bonds is lower than at room temperature because of the change in bond length. With increasing temperature, also the kinetic energy of atoms increases leading to a wider fluctuation in the Morse potential well. This potential well is non-symmetric (Figure 27) [45] which means that, a higher kinetic energy leads to an increase in the average internuclear separation. The increase in the average internuclear separation in turn decreases the energy needed for the polarisation of the bonds and thus the measured Raman shift.

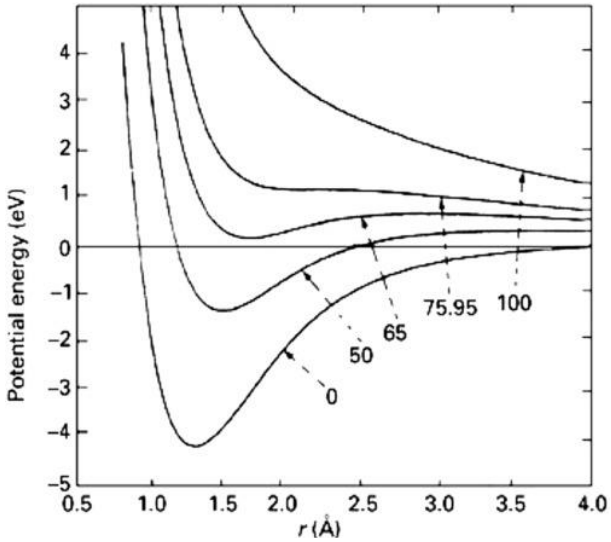

Figure 27 Internuclear spacing described by the Morse potential [45]

The peak position shift at 900°C can be so large that certain close peaks can be mixed up in the peak identification step. For example, the Q1 peak, which is located at 911[cm^{-1}] at room temperature is shifted to 895[cm^{-1}] and therefore can be mistaken for the Q0 peak. To avoid these misinterpretation mistakes the dominant peak's shifts were closely studied. In most of the high temperature measurements the Q1 peak was dominant what is due to the presence of the cuspidine structure at the measurement point. The temperature induced Q1 peak position shift is depicted in Figure 28. The peak position is non-linearly dependent on the temperature because the bond length is also nonlinearly dependent on temperature.

The peak position shift can be the result of other physical effects like pressure or strain, but in the current case the pressure was atmospheric, and no external strain was applied to the samples thus the observed peak position shift was assumed to be the result of the temperature change.

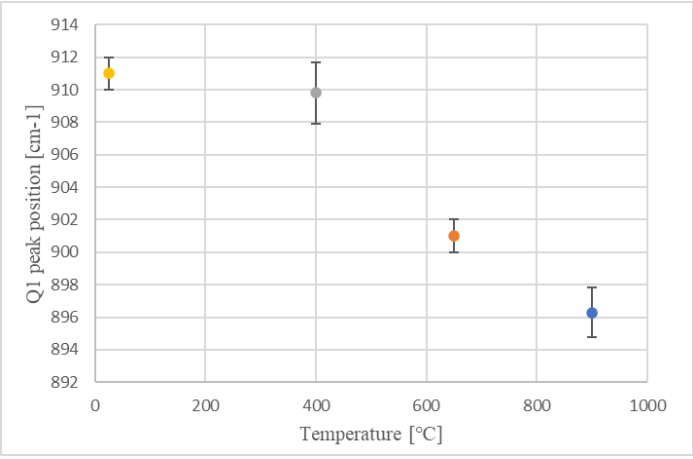

Figure 28 Temperature dependence of the Si-O (Q1) bond shown by the peak position change in the Raman spectrum

Apart of the spectra quality and peak position shifts the only main difference between the room and high temperature spectra is the peak present at the 2350-2450 [cm^{-1}] region. This peak is not present in most high temperature cases, while it is almost always present in the room temperature cases. This indicates a change that takes place during cooling, but the peak

cannot be assigned inconclusively to a specific bond vibration therefore the proposed explanations are discussed in more detail in Appendix 3: Raman spectrum band assignment proposals.

5.1.3. Phase formation

During cooling first, the cuspidine crystals solidify. This was expected from the thermodynamical calculations (Figure 25) because cuspidine is stable at higher temperatures than combeite. Researchers found that pure cuspidine can be stable at high as 1683±10K [46]. Second, the combeite phase crystallises and then finally the amorphous phase. This solidification sequence is confirmed by the crystal morphology with the cuspidine forming large, faceted crystals and the combeite forming a small dendritic structure. In Figure 29 the average Q^2 Q^1 peak intensity ratio is plotted in time. This figure shows that structural changes still took place after reaching the 900°C-isothermal holding temperature because the ratio changed with an approximate linear growth. In the 650°C case no change was observed in the ratio which means that no significant change took place during this time in the cuspidine to combeite ratio assuming the Q^2 Q^1 peaks intensity represent the combeite and cuspidine in the sample. This assumption is based on the fact the cuspidine structure contains Si atoms with one bridging and 3 non bridging atoms, the combeite structure contains Si atoms with 2 bridging and 2 non bridging atoms therefore their ratio change would be visible as a Q^2/Q^1 ratio change. Based upon previous research carried out on similar, F containing mould slags [14] it was expected that structural changes that influence the intensity (Figure 18) and relative ratio (Figure 29) of the Q peaks will take place after the initial Raman measurement too. This was not the case, because no significant structural changes were observed in RS which emphasise the importance of experimental testing of mould slags. Experimental testing is needed because the chemical composition, given by the mould powder manufacturer is not enough to predict the solidification behaviour and structure of mould slags. <1wt% of additions can influence the whole continuous casting process because similar mould slags might behave differently therefore testing should be regularly done for quality control and extensively done for new mould slag development. The Raman spectra collected at 400°C were too noisy to provide calculation basis for such an analysis therefore these data points were excluded from Figure 29.

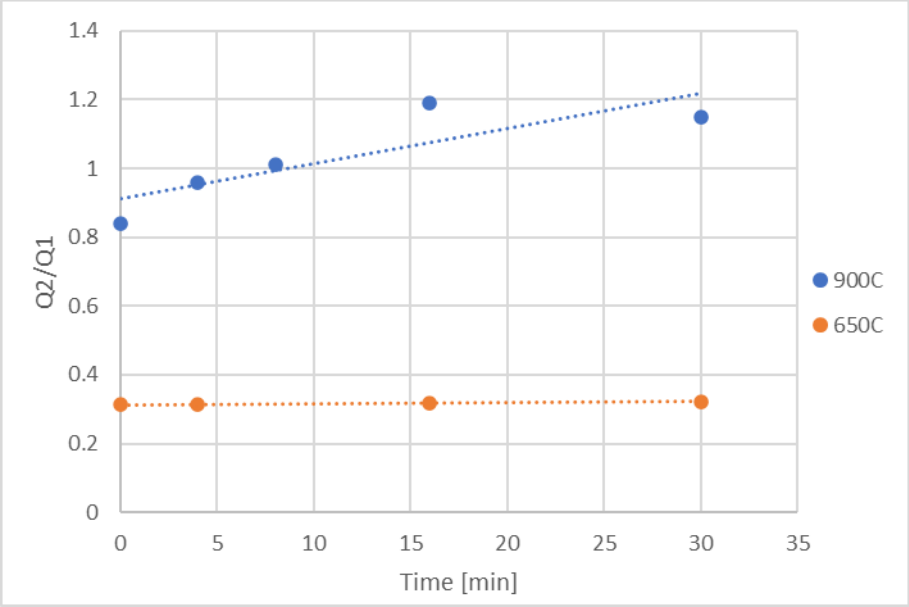

Figure 29 Relative Raman peak intensity changes of two different types of Si-O bonds (Q1, Q2) during isothermal holding

5.2. Characterisation methods

In this research Raman microscopy was utilized for mould slag research in order to identify the forming phases, measure the phase ratios, map the morphology, and finally detect transition metal oxides. This was done both at room and high temperatures.

The phase identification was only a partial success, because purely based upon the Raman results, only the amorphous phase and the cuspidine phase could be identified. At high temperatures this distinction could only be made with the room temperature results in mind, because the high temperature results were low in quality compared to the room temperature ones. For the accurate phase identification XRD measurements were used. There are similarities in the phase identification step of XRD and RS after spectrum collection, because in both cases it is done by matching a set of characteristic peaks to a library of peaks which belong to previously measures or calculated materials. Therefore, the effectiveness and accuracy difference between the two methods, in big part, is caused by the smaller library size of RS results. Overcoming this limitation by measuring the pure mould slag samples will allow RS to be used as a phase identification tool for mould slags.

Because there is no Raman spectrum available in the databases about combeite, instead of the per phase phase-ratio, the overall crystalline ratio was calculated from the RS results. This could be done with the previously explained MLR method with level of accuracy of the SEM based approximation. The accuracy, and the dispersion of the results can be further improved with the accurate pure phase Raman spectra of the different constituent phases.

NiO was the only transition metal oxide on the mould slag samples, and it wasn't there before the sample handling. NiO wasn't present during the RS measurements and wasn't detected. NiO is detectable by RS [47] therefore, Raman microscopy is suitable for this purpose.

The RS mapping measurements' accuracy can be changed by changing the step size of the mapping measurement. Large morphological features like the cuspidine crystals can be

directly observer by RS with a low step size. Smaller sized features like the combeite dendrites which can be less than 0.1 μm thick cannot be directly observed as in the SEM because RS with the setup used in this research have a laser spot size of 1,3 [μm]. This deficiency can be partially overcome by taking a smaller step size than the spot size and post processing the results or by changing the objective or the laser wavelength. In the post processing the measurement, or image, points can be coloured according to the phase ratio gradient of a given phase, thus revealing smaller features than what is directly observable.

Raman microscopy, compared to well established characterisation techniques like XRD is a relatively new technique which is still in its development phase in all the fields of apparat, software, and interpretation. Despite this limitation, this research showed that already in its current state it can provide valuable information about the heat transfer controlling structural parameters of mould slags. Many of the current limitations can be overcome in the future but mould slag research will remain a field which require multi technique characterisation. Raman microscopy offers a streamlined characterisation route for mould powders, but other techniques will be also needed in the future due to the complex nature of the heat transfer phenomena across the mould slag layer where both surface [48] and bulk [49] properties play a role.

5.3. Influence on the casting process

The high temperature formation of cuspidine means that in the early stages of the casting, meaning on the upper part of the mould where the temperature is higher, the heat transfer behaviour will be mostly controlled by the cuspidine formation. After the early formation of cuspidine, combeite also formed from the remaining liquid slag which means that after the early stages, the change of the mould slags heat transfer behaviour is caused by the combeite formation till the end of solidification. After the end of solidification, the heat transfer behaviour change is caused by the temperature dependence of the constituents' heat transfer coefficient [50].

6. Conclusion and recommendations

The S1 continuous casting mould slag is a multi-component system, made of several different minerals with varying chemical composition. Mould slags go through several phase changes during the continuous casting process, both during melting and solidification therefore their behaviour should be studied during the whole cycle. The phase changes result in a varying thermal conductivity that depends both on the temperature and the temperature history. Macroscopically the heat transfer of the mould slag is determined by the main phase types, the phase ratios, metal oxide distribution, and crystal morphology.

In the operating temperature window of the mould slags during cooling, which is between 1200 – 300 °C, the S1 mould slag can take one or the mixture of the following phases: liquid slag, amorphous glass, cuspidine, combeite. In theory other minor phases can be also present in the solidifying mould slag, but these phases were not detected in heat transfer wise relevant quantities by any of the applied characterisation methods.

After the 1-hour long isothermal holding the overall crystalline ratios were measured by different characterisation methods. Three calculation methods were used to determine the overall crystalline ratios by Raman spectroscopy. Out of these three the multi linear regression method was the most accurate with the following results: $X_{900°C}$= 73±8%, $X_{900°C}$=81±11%, $X_{900°C}$=77±8%. These results are within the SEM approximation result's measurement error.

No distinct transition metal oxide phases were detected except the nickel oxide particles which are not part of the mould slag structure. The nickel oxide particles are contaminations that got detached from the sample holder in between the experiments and that is why they were not detected in the Raman spectroscopy, only in the XRD and SEM after the sample transfer, thus contamination effect, took place.

The mould slags have a complex and interconnected structure after solidification. The cuspidine phase crystallises in roughly 5 – 25µm long faceted crystals. These cuspidine crystals are surrounded by a matrix which is a mixture of small, ~0,25µm dendritic combeite crystals and amorphous glass.

The crystallisation speed of the S1 mould slag was higher during the current experiments, than expected from previous research [14]. Especially in case of the 650°C samples where no significant change was observed in the Q^2/Q^1 ratio. The morphology showed that first the cuspidine crystallises than the combeite.

Multi method characterisation is essential in mould slag research. From heat transfer perspective wise, the four main structural features (phase type, ratio, metal oxides, morphology) cannot be accurately determined with only one technique because of the structure's complex nature. In this research Raman spectroscopy was used parallel to characterisation methods traditionally used to assess the previously mentioned four structural features. The comparison of these results showed that Raman spectroscopy can provide additional information, and it can potentially measure all four of the features but with the methods current accuracy, other supplementary techniques are needed to properly determine the mould slag's structure.

Raman spectroscopy as a technique can be improved in the future to accurately measure all four, heat transfer behaviour wise relevant, structural features. The phase detection aspect can be fulfilled by Raman spectroscopy, by synthetizing and measuring all of the unique, pure constituent phases. Knowing the accurate Raman spectrum of each pure phase, the mixture spectra can be also identified. The pure spectra would also improve the accuracy of the MLR phase fraction calculations. The pure phase spectra would also allow researchers to use computation programs to increase the resolution of mapping Raman images, which might provide the opportunity to study the morphology of mould slags with Raman microscopy too.

Improvements can be achieved on the experimental side too. Introducing a laminar air flow to the reaction cell through the heating phase would minimalize the F contamination of the AlO glass of the cell leading to a better spectrum quality at high temperatures. Further modifying the reaction cell to accommodate a heating-cooling system which can achieve a wider range of heating and cooling speeds would greatly broaden the application possibilities of Raman spectroscopy in the field of mould slag research.

In conclusion, Raman spectroscopy was proven to be a powerful and quick characterisation method for mould slag studies. As this technique is relatively new in this research field compared to other techniques like XRD or SEM, substantial improvement can be achieved in the future, but the currently obtainable results already proved to be insightful.

References

1. https://worldsteel.org/media/press-releases/2023/worldsteel-short-range-outlook-october-2023/ (visited: 13.06.2024.)
2. Somers, J. (2022): Technologies to decarbonise the EU steel industry. Publications Office of the European Union, Luxembourg, doi:10.2760/069150
3. Alan Cramb (2003): The Making, Shaping and Treating of Steel – Casting Volume, The AISE Steel Foundation, Pittsburgh, Pa.
4. Brimacombe Continuous Casting Course. Continuous Casting of Steel Billets, Blooms and Slabs. May 2008. 1133 West Hastings Street, Vancouver, B.C. Canada V6E 3T3
5. Lance C. Hibbeler (2009). Thermo-mechanical Behaviour During Steel Continuous Casting in Funnel Molds. Master's Thesis. University of Illinois at Urbana-Champaign
6. Lance C. Hibbeler (2014). Multiphysics Modelling of the steel continuous casting process. PhD Thesis. University of Illinois at Urbana-Champaign
7. Mills, K. C., & Däcker, C. (2017). The Casting Powders Book. In Springer eBooks. https://doi.org/10.1007/978-3-319-53616-3
8. Allibert, M. (1995). *Slag Atlas*.
9. Shelby, J. E. (2005a). Introduction to glass science and technology. Royal Society of Chemistry.
10. Zhang, B., Tekle, H., O'Malley, R. J., Sander, T. P., Smith, J. D., Gerald, R. E., & Huang, J. (2023). In situ and Real-Time mold flux analysis using a High-Temperature Fiber-Optic RAMAN sensor for steel manufacturing applications. Journal of Lightwave Technology, 41(13), 4419–4429. https://doi.org/10.1109/jlt.2023.3239428
11. Advanced Science News. (2016, November 17). Reducing the energy consumption of ironmaking. https://www.advancedsciencenews.com/reducing-energy-consumption-ironmaking/
12. Zachariasen, W. H. (1932). THE ATOMIC ARRANGEMENT IN GLASS. Journal of the American Chemical Society, 54(10), 3841–3851. https://doi.org/10.1021/ja01349a006
13. Pauling, L. (1939). The nature of the chemical bond.
14. Peterson, E & Sander, T & Smith, Jeffrey & O'Malley, Ronald. (2017). Investigation of Mold Flux Crystallization by Rapid Quenching and Isothermal Aging in Molten Tin.
15. Kromhout, J. A., Dekker, E., Kawamoto, M., & Boom, R. (2013). Challenge to control mould heat transfer during thin slab casting. Ironmaking & Steelmaking, 40(3), 206–215. https://doi.org/10.1179/1743281212y.0000000030
16. Liu L, Han X, Li M, Zhang D. Influence of Mineralogical Structure of Mold Flux Film on Heat Transfer in Mold during Continuous Casting of Peritectic Steel. Materials. (2022) Apr 20, Basel;15(9):2980. https://doi.org/10.3390/ma15092980
17. Hideaki Yamamura, Norimasa Yamasaki, Toshiyuki Kajitani, Satoru Mineta, Junji Nakashima. (2013). Clarification and Control of the Heat Transfer Phenomenon in the Mold and Strand of Continuous Casting Machines. Nippon Steel Technical Report No. 104.

18. Andersson, S. P., & Eggertson, C. (2014). Thermal conductivity of powders used in continuous casting of steel. Ironmaking & Steelmaking, 42(6), 456–464. https://doi.org/10.1179/1743281214y.0000000250
19. Takahasi S., Ito J. (2019) Fluorine Free Mold Powder. Shinagawa technical Report Vol. 62.
20. Sridhar, S., Mills, K. C., Afrange, O., Lörz, H., & Carli, R. (2000). Break temperatures of mould fluxes and their relevance to continuous casting. Ironmaking & Steelmaking, 27(3), 238–242. https://doi.org/10.1179/030192300677534
21. Schnickmann, A., Hampel, S., Schirmer, T., & Fittschen, U. E. A. (2023). Formation of Lithium-Manganates in a complex SLAG system consisting of LI2O-MGO-AL2O3-SIO2-CAO-MNO—A first survey. Metals, 13(12), 2006. https://doi.org/10.3390/met13122006
22. Larkin, P. J. (2011). Infrared and Raman spectroscopy: Principles and Spectral Interpretation. Elsevier Science Limited.
23. Bagheri, M., Komsa, HP. High-throughput computation of Raman spectra from first principles. Sci Data 10, 80 (2023). https://doi.org/10.1038/s41597-023-01988-5
24. Database of Raman spectroscopy, X-ray diffraction and chemistry of minerals. (n.d.). https://rruff.info/
25. Fran A. (2019) Measurement of the Temperature Dependence of Water Using a Near-Infrared Raman Spectrograph. Spectroscopy Spectroscopy Volume 34 Issue 6 Pages: 10–15
26. Kim, G. H., & Sohn, I. (2013). Role of B2O3 on the viscosity and structure in the CAO-AL2O3-NA2O-Based system. Metallurgical and Materials Transactions B-process Metallurgy and Materials Processing Science, 45(1), 86–95. https://doi.org/10.1007/s11663-013-9953-2
27. Matsushita, T., Sasaki, Y., Görnerup, M., & Seetharaman, S. (2006). Stress relaxation behavior of molten slags. Isij International, 46(8), 1258–1263. https://doi.org/10.2355/isijinternational.46.1258
28. Fan, L., Liu, C., & Jiang, M. (2022). Crystallization characteristics and structural analysis of CaO–SiO2-based mold fluxes with different La2O3 contents (2022). Ceramics International, 48(8), 11527–11534. https://doi.org/10.1016/j.ceramint.2022.01.008
29. Park, J. H. (2012). Structure-Property Correlations of CaO-SiO2-MnO Slag Derived from Raman Spectroscopy. Isij International, 52(9), 1627–1636. https://doi.org/10.2355/isijinternational.52.1627
30. Ko, K. Y., & Park, J. H. (2013). Effect of CAF2 addition on the viscosity and structure of CAO–SIO2–MNO SLAGS. Isij International, 53(6), 958–965. https://doi.org/10.2355/isijinternational.53.958
31. Zhang, B., Tekle, H., O'Malley, R. J., Sander, T. P., Smith, J. D., Gerald, R. E., & Huang, J. (2023). In situ and Real-Time mold flux analysis using a High-Temperature Fiber-Optic RAMAN sensor for steel manufacturing applications. Journal of Lightwave Technology, 41(13), 4419–4429. https://doi.org/10.1109/jlt.2023.3239428
32. Seo, M., Shi, C., Wang, H., Cho, J., & Kim, S. (2015). Non-isothermal melt crystallization of cuspidine in CaO–SiO2–CaF2 based glasses. Journal of Non-Crystalline Solids, 412, 58–65. https://doi.org/10.1016/j.jnoncrysol.2015.01.008
33. inVia™ InSpect confocal Raman microscope (renishaw.com) (visited: 22.05.2024.)

34. Plc, R. (n.d.). Renishaw: Raman software. Renishaw. https://www.renishaw.com/en/raman-software--9450
35. Menges, F. (n.d.). Spectragryph - optical spectroscopy software. Spectroscopy. https://www.effemm2.de/spectragryph/
36. Liu, H., Kaya, H., Lin, Y., Ogrinc, A., & Kim, S. H. (2021). Vibrational spectroscopy analysis of silica and silicate glass networks. Journal of the American Ceramic Society, 105(4), 2355–2384. https://doi.org/10.1111/jace.18206
37. https://rruff.info/Cuspidine/R060049 (visited: 05.05.2024.)
38. Kim, G. H., & Sohn, I. (2013). Role of B2O3 on the viscosity and structure in the CAO-AL2O3-NA2O-Based system. Metallurgical and Materials Transactions B, 45(1), 86–95. https://doi.org/10.1007/s11663-013-9953-2
39. Qiuhan L., Shufeng Y., Yanling Z., Zhuoqing A., Zhancheng G. (2017): Effects of MgO, Na2O, and B2O3 on the Viscosity and Structure of Cr2O3-bearing CaO–SiO2–Al2O3 Slags. 017), No. 4 689. 2017 ISIJ ISIJ International, Vol. 57 (2017), No. 4, pp. 689–696
40. Marsich, L., Moimas, L., Sergo, V., & Schmid, C. (2009). Raman spectroscopic study of bioactive silica based glasses: The role of the alkali/alkali earth ratio on the non-bridging oxygen/bridging oxygen (NBO/BO) ratio. Spectroscopy, 23, 227–232. https://doi.org/10.3233/spe-2009-0380
41. Juroszek, R., Krüger, B., Galuskina, I., Krüger, H., Tribus, M., & Kürsten, C. (2019). Raman Spectroscopy and Single-Crystal High-Temperature investigations of bentorite, Ca6Cr2(SO4)3(OH)12·26H2O. Minerals, 10(1), 38. https://doi.org/10.3390/min10010038
42. Osipov, A. A. (2019). High-temperature Raman spectroscopy. Pure and Applied Chemistry, 91(11), 1749–1756. https://doi.org/10.1515/pac-2019-0115
43. Baldorj, B., Wagner, T., & Markl, G. (2023). A fluid inclusion and stable-isotope study of hydrothermal vein mineralization, Schwarzwald district, Germany. Геологийн Асуудлууд, 16, 5–31. https://doi.org/10.22353/.v16i1.2258
44. Koga, K. T., Garrido, C. J., Padrón-Navarta, J. A., Sánchez-Vizcaíno, V. L., & Gómez-Pugnaire, M. T. (2014). FTIR and Raman spectroscopy characterization of fluorine-bearing titanian clinohumite in antigorite serpentinite and chlorite harzburgite. Earth Planets and Space, 66(1). https://doi.org/10.1186/1880-5981-66-60
45. Encyclopedia of Spectroscopy and Spectrometry. (2016). Academic Press.
46. Watanabe, T., Fukuyama, H., Nagata, K., & Susa, M. (2000). Phase diagram cuspidine (3CaO · 2SiO2 · CaF2)-CaF2. Metallurgical and Materials Transactions B, 31(6), 1273–1281. https://doi.org/10.1007/s11663-000-0015-1
47. NiO raman spectrum | Raman for life. (n.d.). https://ramanlife.com/library/nickel-oxide/
48. Hideaki Yamamura, Norimasa Yamasaki, Toshiyuki Kajitani, Satoru Mineta, Junji Nakashima. (2013). Clarification and Control of the Heat Transfer Phenomenon in the Mold and Strand of Continuous Casting Machines. Nippon Steel Technical Report No. 104.
49. Andersson, S. P., & Eggertson, C. (2014). Thermal conductivity of powders used in continuous casting of steel. Ironmaking & Steelmaking, 42(6), 456–464. https://doi.org/10.1179/1743281214y.0000000250

50. Huang, S., Wang, Z., Wang, F., Liu, F., & Barati, M. (2022). Heat transfer properties and molecular mechanisms of cuspidine (Ca4Si2O7F2): An atomic-scale molecular dynamics study. Chemical Engineering Science, 253, 117594. https://doi.org/10.1016/j.ces.2022.117594
51. https://atlassteels.com.au/wp-content/uploads/2021/06/Stainless-Steel-310-310S-310H-Grade-Data-Sheet-23-04-21.pdf (visited: 03.04.2024.)
52. https://www.atlassteels.com.au/documents/Atlas_Grade_datasheet_316_rev_Jan_2011.pdf (visited: 03.04.2024.)
53. https://salomons-metalen.nl/datasheets/Nickel_200_201.pdf (visited: 03.04.2024.)
54. https://salomons-metalen.com/datasheets/Alloy_400.pdf (visited: 03.04.2024.)
55. https://salomons-metalen.com/datasheets/Alloy_600.pdf (visited: 03.04.2024.)
56. https://nickelinstitute.org/media/4124/alloy-selection-for-service-in-hydrogen-fluoride-hydrofluoric-acid-and-fluorine-10074.pdf (visited: 03.04.2024.)
57. Mattioli, Michele & Giordani, Matteo & Ballirano, Paolo & Salvioli Mariani, Emma & Bernardini, Simone & Ventura, Giancarlo. (2023). First occurrence, crystal-chemistry and structure of erionite, a carcinogenic fibrous zeolite, from the volcanic rocks of Latium (Italy). Periodico di Mineralogia. 92. 159-178. 10.13133/2239-1002/18084.
58. Frost, R. L. (2004). Raman microscopy of selected chromate minerals. Journal of Raman Spectroscopy, 35(2), 153–158. https://doi.org/10.1002/jrs.1121
59. Buzgar, Nicolae & Apopei, Andrei. (2014). The Raman study of certain carbonates. 10.13140/2.1.1358.3368.
60. Frost, R. L., Palmer, S. J., & Grand, L. (2010). Raman spectroscopy of gallium-based hydrotalcites of formula Mg6Ga2(CO3)(OH)16· 4H2O. Journal of Raman Spectroscopy, 41(7), 791–796. https://doi.org/10.1002/jrs.2508
61. Nandi, R., Singh, S. K., Singh, H. K., Rao, D. S. S., Prasad, S. K., Singh, B., & Singh, R. K. (2016). Molecular approach to phase transitions in a calamitic ester substituted aroylhydrazone liquid crystal. Journal of Raman Spectroscopy, 47(9), 1095–1101. https://doi.org/10.1002/jrs.4933
62. Lavrov, E. V., Weber, J., Huang, L., & Nielsen, B. B. (2001). Vacancy-hydrogen defects in silicon studied by Raman spectroscopy. Physical Review. B, Condensed Matter, 64(3). https://doi.org/10.1103/physrevb.64.035204
63. Hai-Wen, Li & Kikuchi, Kentaro & Sato, Toyoto & Nakamori, Yuko & Ohba, Nobuko & Aoki, Masakazu & Miwa, Kazutoshi & Towata, Shin-ichi & Shin-ichi, Orimo. (2008). Synthesis and Hydrogen Storage Properties of a Single-Phase Magnesium Borohydride Mg(BH4)(2). Materials transactions. 49. 2224-2228. 10.2320/matertrans.MA200807.
64. Richard, Jason & Cid, Sonia & Rouquette, Jerome & Lee, Arie & Bernard, Samuel & Haines, Julien. (2016). Pressure-Induced Insertion of Ammonia Borane in the Siliceous Zeolite, Silicalite-1F. The Journal of Physical Chemistry C. 120. 10.1021/acs.jpcc.6b02134.

Appendix 1: Raman spectroscopy measurement details

The detailed environmental and other parameters of the Raman spectroscopy measurements are shown in Table 11.

Table 11 Detailed Raman spectroscopy measurement environmental details

Sample name	Sample type	Date of measurement	Lab temperature [℃]	Humidity [%]	Sample holder	Sample weight [g]
T1_S1_Ta_RT1-1200-400-RT2_3011	S1	30.11.2023.	-	-	Ta	M
T2_S1_RT_2603	S1	26.03.2024.	23.9	33	Al	L
T3_S2_RT_	S2		24.1	30	Al	L
T4_Ta_RT1-900-RT2_1504	-	15.04.2024.	23.7	38	Ta	-
T5_TaBN_RT1-1200-RT2_2204	-	22.04.2024.	24.3	30	TaBN	-
T6_S1_TaBN-RT1-1200-RT2_2204	S1	22.04.2024.	24.3	30	TaBN	S
T7-S2_TaBN-RT1-1200-RT2_2304	S2	23.04.2024.	23.9	28	TaBN	S
T8_S1_Ni_RT1-1200-RT2_2405	S1	24.05.2024.	24.5	48	Ni	S
T9_S1_Ni-RT1-1200-650-RT2_2805	S1	28.05.2024.	24.1	46	Ni	M
T10_Ni_RT1-1200-900-650-400-RT2_3005	-	30.05.2024.	24.3	49	Ni	-
E1_S1_Ni_RT1-1200-400-RT2_0306	S1	03.06.2024.	24.0	45	Ni	S
E2_S1_Ni_RT1-1200-650-RT2_0706	S1	07.06.2024.	23.7	44	Ni	L
T11_S1_Ni_RT1-1200-900-600-RT2_0706	S1	07.06.2024.	23.7	44	Ni	M
E3_S1_Ni_RT1-1200-900-RT2_100C/s_1106	S1	11.06.2024.	24,3	41	Ni	M
E4_S1_Ni_RT1-1200-900-RT2_1306	S1	13.06.2024.	24,4	42	Ni	S

E5_S1_Ni_RT1-1200-650-RT2_1406	S1	14.06.2024.	25	44	Ni	M
E6_S1_Ni_RT1-1200-400-RT2_0807	S1	08.07.2024.	24,5	49	Ni	s
E7_S1_Ni_RT1-1200-900-RT2_0907	S1	09.07.2024.	24,3	51	Ni	M
E8_S1_Ni_RT1-1200-RT2_0907	S1	09.07.2024.	25,2	51	Ni	M
E9_S2_Ni_Rt1-1200-900-RT2_15_07_2024	S2	15.07.2024.	24.0	51	Ni	M
E10_S1_RT1-1350-RT2_16_07_2024	S1	16.07.2024.	23.9	56	Ni	M

Sample name meaning experiment type [T-trial, E-experiment] number_ material_ sample holder_ temperature program_ date. Sample weight coding: S = 0.0064±0.001g, M = 0.0098±0.005g, L = 0.0127±0,005g. Sample holders: Ta – tantalum TaBN – tantalum holder with a spray-painted boron nitride coating layer, Ni – nickel, Al – aluminium.

The temperature programs and follow up experiments by sample are shown in Table 12.

Table 12 Temperature programs and follow-up experiments of each heat-treated sample

Name	Temperature program	Follow-up experiments
T1	25-400-25	-
T9	25-650-25	-
E1	25-400-25	XRD
E2	25-650-25	SEM, XPS
E3	25-900-25	SEM
E4	25-900-25	XRD
E5	25-650-25	XRD
E6	25-400-25	SEM
E7	25-900-25	SEM
E8	25-1200-25	SEM
E9	25-900-25	SEM
E10	25-1350-25	SEM

Appendix 2: Sample holder material selection

Minimal requirements:

- High melting point (>1300℃)
- Formable
- Available
- Low price

Additional requirements:

- High corrosion resistance in F and Na containing substances
- Should not contain the same elements as the mould slags
- Low diffusion rate in most materials

Five possible candidates were chosen which fulfil the minimal requirements. These are the stainless-steel alloys of SS 310 and SS 316 and the nickel alloys of Ni 201, Ni 400 and Ni 600 Table 13. Considering all of the requirements, the Ni 201 alloy was chosen due to its overall performance.

Table 13 Proposed sample holder material options and their relevant material properties

Name	SS 310 [52, 56]	SS 316 [52,56]	Ni 201 [54,56]	Ni 400 [54,56]	Ni 600 [55 56]
Composition [%]	Fe - 53, Ni - 20, Cr - 25, Si - 1, C – 0,1	Fe - 68, Cr – 16, Ni – 12, Mo – 2,5, Si – 1, C – 0.07	Ni - 99	Ni-65, Cu - 35	Ni – 72, Cr – 15, Fe - 10
Melting range [°C]	1400 - 1455	1390-1440	1435-1446	1300-1350	1354-1413
YS - UTS [MPa]	205-515	205-515	105-520	207-586	172-1700
Elongation [%]	40	40	55	45	35-55
Corrosion resistance	Resist fuming nitric acid at room temperature and fused nitrates up to 425°C.		NaOH: resistance: (0.025mm/a) Withstands oxidizing atmospheres up to 1100°C	Good resistance to hydrofluorineic acid.	Better oxidation resistance than pure Ni

Appendix 3: Raman spectrum band assignment proposals

Raman spectroscopy is a relatively new characterisation method in mould slag research. Therefore, accurate band assignment in most cases is not possible based purely upon experimental results. In case of the S1 mould slag a number of the peaks in the Raman spectrum are accurately identifiable but not all. In this study a detailed Raman spectroscopy experimental plan was carried out which identified 20+ reoccurring Raman peaks. Extensive literature study was carried out to identify the peaks, but in many cases de peak identification was not conclusive. The conclusive results were shown in previous chapters. As mould slag research is still an area of interest, the non-conclusive, proposed band assignments are explained in this appendix to aid further research.

The 138±4 [cm^{-1}] peak might be identified as the lattice mode vibration of the Zeolite structure [57]. Zeolite is a aluminosilicate mineral. This means that this peak shows the presence of aluminium in the given measurement point. Both Si and O are present in the structure therefore the 354±5 [cm^{-1}] peak is a vibration mode of SiO [5837].

The peaks at 1494±4 [cm^{-1}], 1690±5 [cm^{-1}], 1998±4 [cm^{-1}], 2166±4 [cm^{-1}], 2413±3 [cm^{-1}], 2676±5 [cm^{-1}], and at 2849±5 [cm^{-1}] all belong to the crystalline phase. These peaks are also present in the naturally occurring Cuspidine Raman spectra [37] and assigned to the lattice vibrational modes of the crystal. Although the theoretical structure of Cuspidine contains only the following elements: Si, Ca, F, O, Cuspidine is a crystallographic structure thus other elements can be also incorporated into the structure thus leading to Raman bands that occur at the crystalline phase. The 1494±4 [cm^{-1}] Raman peak was identified as CO_3^{2-} antisymmetric stretching modes by Frost et al. [60]. CO_3^{2-} can form during the high temperatures of the experimental cycle thus might be detected in the S1 mould slag sample. Following the same reasoning the 1998±4 [cm^{-1}] peak can be a CO??? vibration [61].

Mould slags are presumed to be a mix of different oxides, but several elements can be in the form of hydroxides too. Based on this assumption, the Raman peaks in the 2150-1900 [cm^{-1}] regions can be hydroxides: 2166±4 [cm^{-1}]; Si-H [62], 2413±3 [cm^{-1}]; B-H [63], 2849±5 [cm^{-1}]; C – H [64].

Peaks in the Raman spectrum can be the result of physical effects too, not only the result of specific bond's Raman effect. To test for this possibility in the 1500-2700 [cm-1] Raman shift region, the E9 sample (S2) was tested with, the same type, but a different Raman microscope using different laser wavelengths. The results of these measurements are shown in Figure 30, Figure 31, and Figure 32. In case of both the 488 [nm] and the 633 [nm] laser measurements, similarly to the 532 [nm] measurements, different type of Raman spectra were observed. In all cases the most dominant Si-O (Q1) peak was clearly observed. The other peaks at the 1000 + [cm^{-1}] Raman shift area was partially observed in the 488 [nm] and 633 [nm] measurements. These results do not completely rule out the possibility of a physical effect.

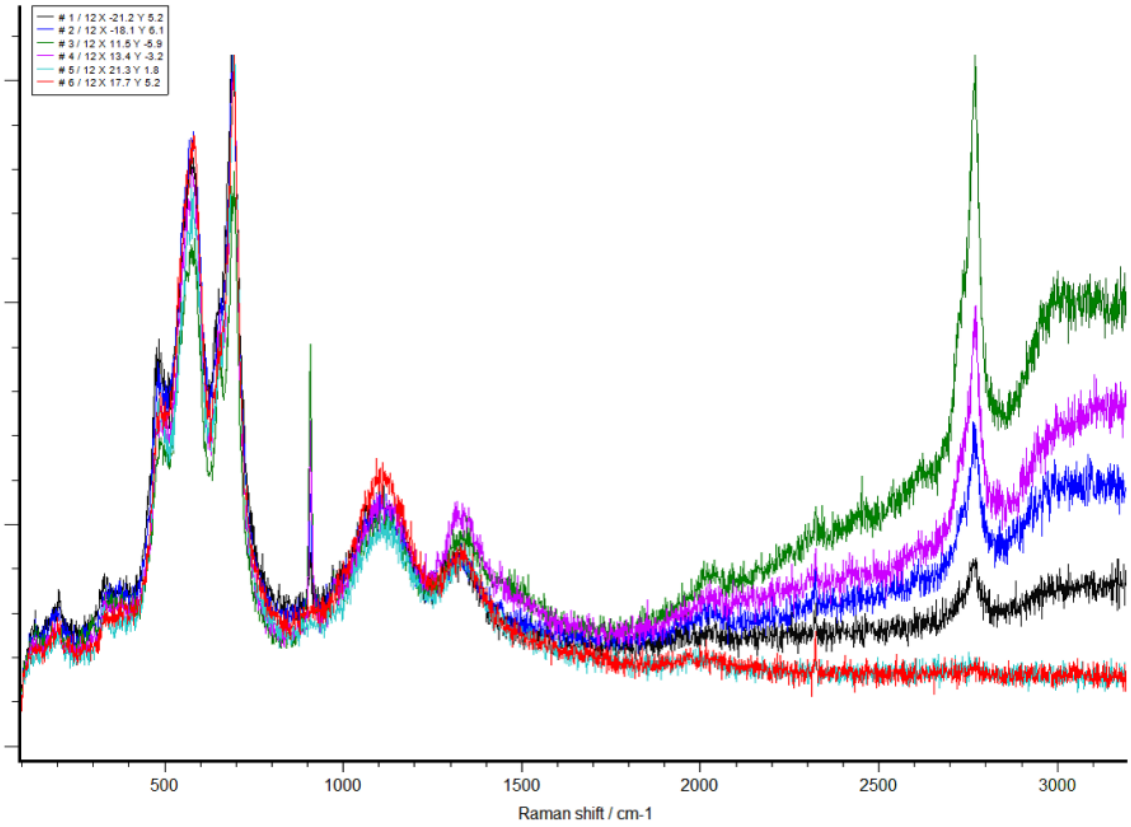

Figure 30 S2 Type 4 Raman spectra of S2 mould slag measured with 488nm laser

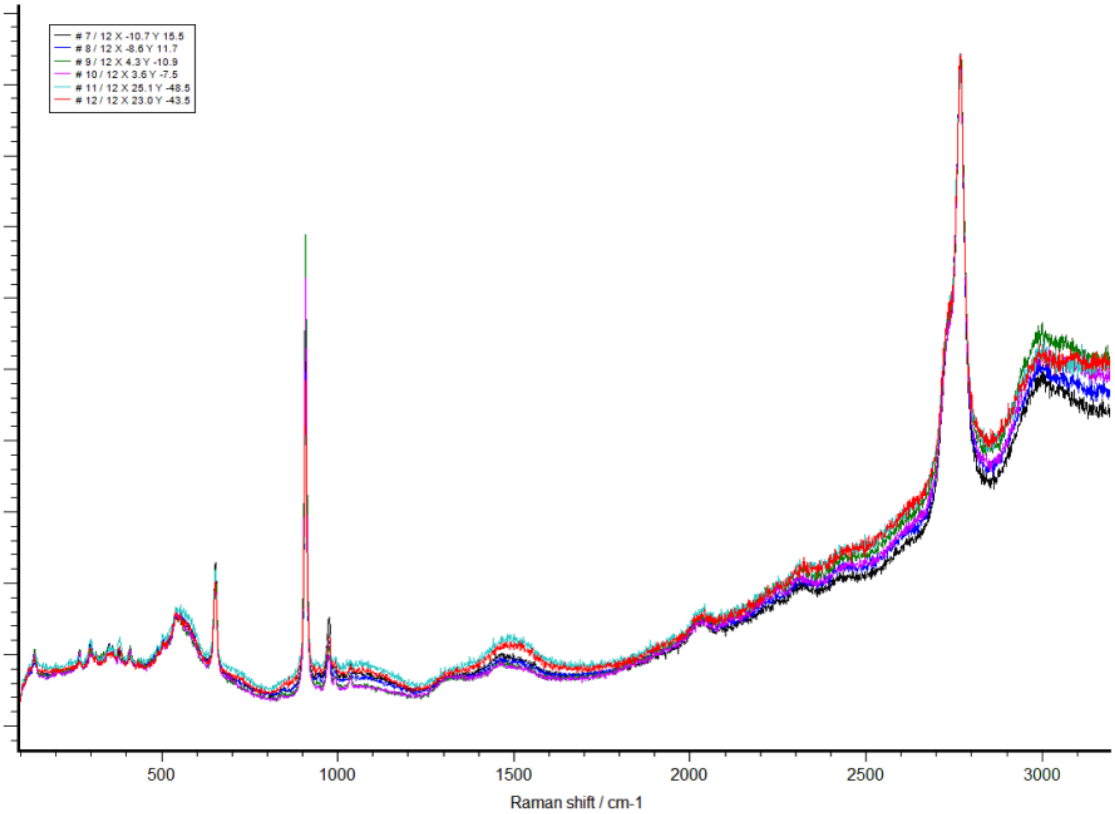

Figure 31 Type 2 Raman spectra of S2 mould slag measured with 488nm laser

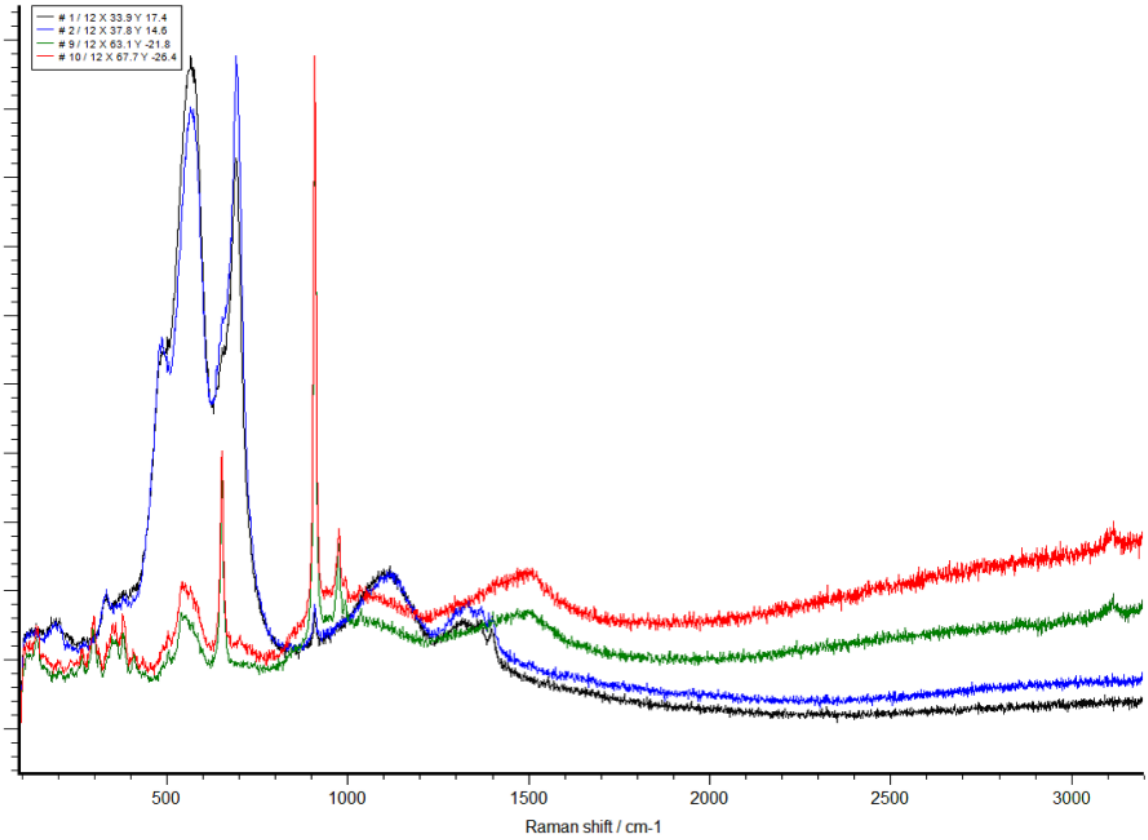

Figure 32 Type 2 and type 4 Raman spectra of the S" mould slag, measured with 633nm laser

Appendix 4: S2 Raman spectroscopy measurement results

To test the applicability of the designed Raman experiment on another mould powder composition, the same experiment was carried out on the S2 mould powder (Table 14).

Table 14 S2 mould powder composition

	S2	
	measured	**standard**
CaO/SiO_2	*0.85*	0.77-0.89
SiO_2	34.1	33.5-35.5
CaO	29.0	28.0-30.0 (=CaO + MgO)
MgO	1.4	
Al_2O_3	4.5	4.0-5.5
Na_2O	11.7	11.5-13.5
K_2O	0.5	
MnO	0	<0.1
Fe_2O_3	1.3	1.0-2.5
F	8.5	8.0-9.5
C_{free}^{*}	*2.1*	*1.5-2.5*
CO_2	8.6	8.5-10.0
C_{total}	4.4	4.0-5.0

The S1 mould powder has a similar composition to S1 with the main difference being the *CaO/SiO_2* ratio and the aluminium content. Due to the similarities, the S2 powder showed similar melting behaviour, with a slightly lower melting point. After the solidification and the isothermal holding, a detailed mapping measurement was carried out similarly to the S1 experiments.

The results showed both similarities and differences with the S1 results. Instead of two, four different Raman spectrum types was observed in case of the S2 mould slag. Type 1 (Figure 33) and 2 (Figure 34) were similar to the type 1 and 2 spectra of the S1 mould slag. The main difference between the two material's type 1 spectra was the Al-O stretching vibration peak at 560±10[cm^{-1}]. The intensity of this peak was higher in case of S2 which points to a higher Al content in the amorphous phase which was expected from the mould powder composition.

After Raman phase identification, the type 3 spectra of S2 were identified as corundum. This was a relatively rare spectra which appeared as a separate island spatially. This means that Al formed its own separate phase in S2 due to its high content. The type 4 spectra of S2 could

not be conclusively identified purely from the spectrum, which further proves the gap in the databases.

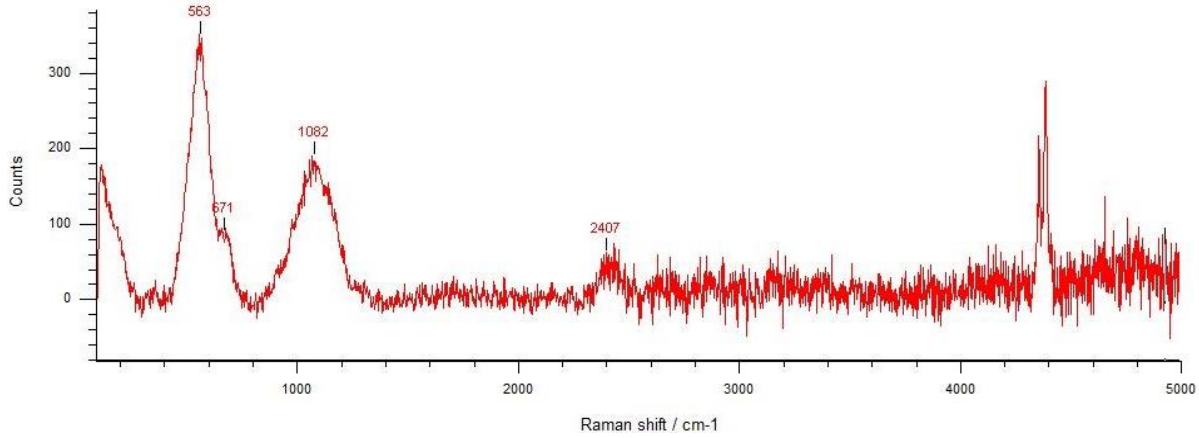

Figure 33 Type 1 Raman spectra of S2 mould slag

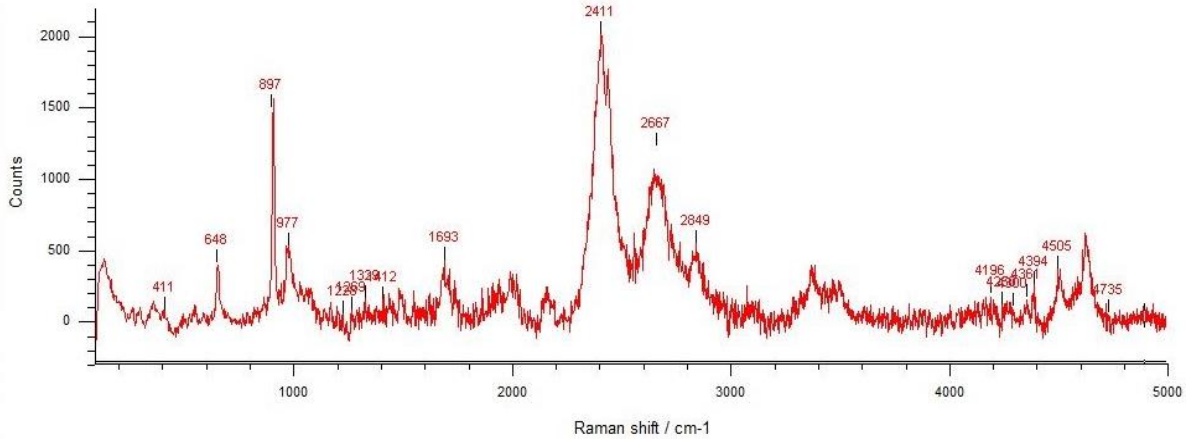

Figure 34 Type 2 Raman spectra of S2 mould slag

Appendix 5: X-ray photoelectron spectroscopy results

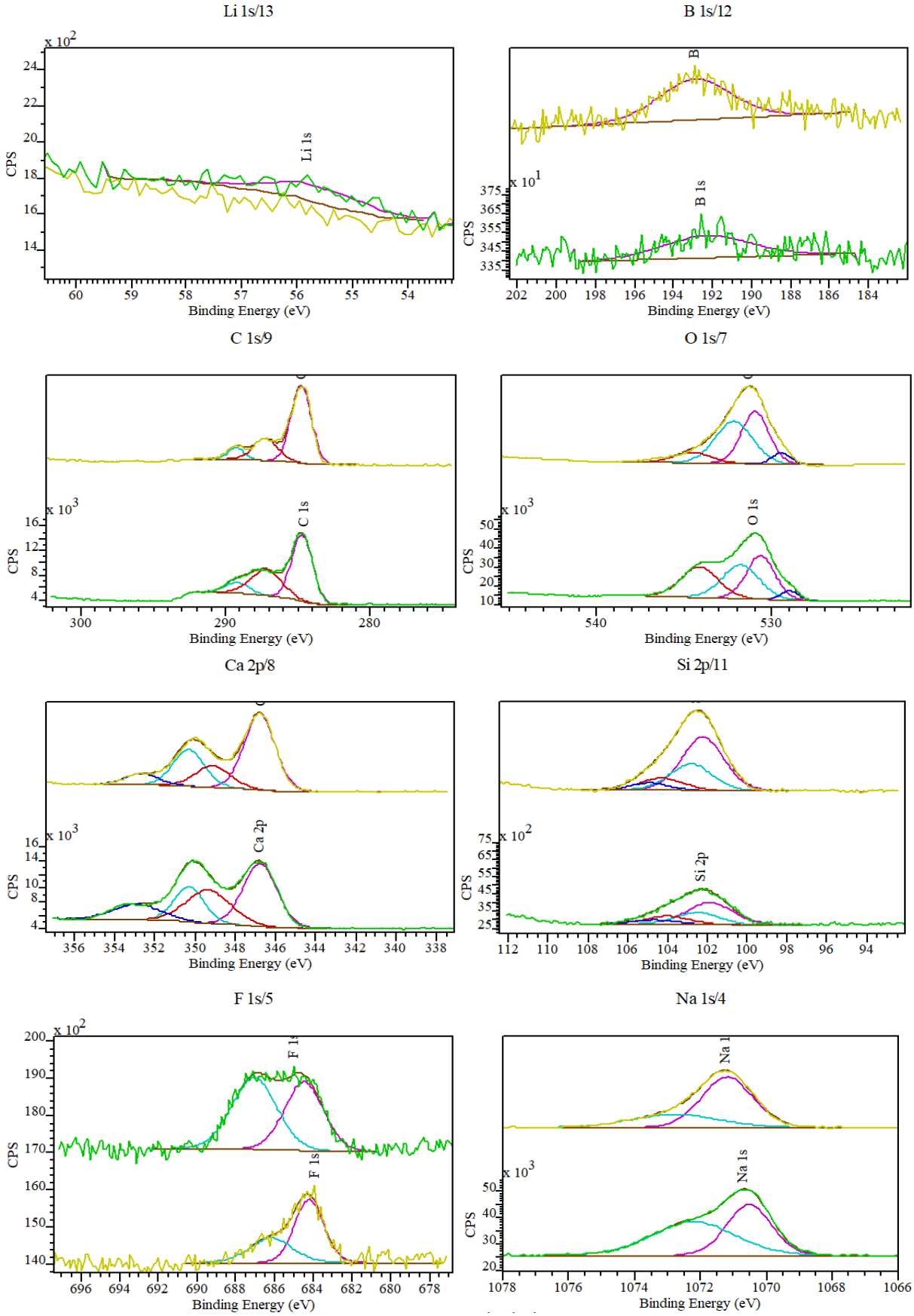

Figure 35 XPS measurement results of E2 sample of the S1 mould slag after a 650˚C heat cycle

The XPS experiments were performed in order to aid the understanding of the Raman spectra in the 1500-300 [cm^{-1}] wavelength ratio. The increasing Raman shifts correspond with decreasing atom sizes that produce the Raman shift. Due to this effect, the XPS measurements were aimed at detecting boron and lithium which can be part of the minerals that are the raw materials of mould powders.

The XPS measurement results are summarised in Figure 35. The two subplots per plot correspond to two different areas measured on the E2 sample. Only the E2 sample was measured by XPS because all samples have the same composition, thus if B or Li is present in one of those, it will be present in the others too.

Lithium was not detected by the XPS measurements; therefore, it is not present on the surface of the mould slag samples. Boron was detected on both measurement areas with a single peak in the XPS spectra which means that it is present on the sample and has one chemical state.

Fluorine and sodium both had two peaks in the XPS spectra, while the other measured elements (O, Ca, Si, C) had several. This means that these elements are detected in several different chemical states. This observation corresponds with the Raman observations because for example Si is detected in 4 chemical states in the XPS, and at least three different Si-O bonds were observed in the Raman spectra (Q1, Q2, Q3 peaks).